Simulation of foam enhanced-oil-recovery processes using operator-based linearization approach

Lyu, Xiaocong; Voskov, Denis; Tang, Jinyu; Rossen, William R.

Important note
To cite this publication, please use the final published version (if applicable).
Please check the document version above.

Simulation of Foam Enhanced-Oil-Recovery Processes Using Operator-Based Linearization Approach

Xiaocong Lyu, Delft University of Technology; **Denis Voskov*,** Delft University of Technology and Stanford University; and **Jinyu Tang** and **William R. Rossen,** Delft University of Technology

Summary

Foam injection is a promising enhanced-oil-recovery (EOR) technology that significantly improves the sweep efficiency of gas injection. Simulation of foam/oil displacement in reservoirs is an expensive process for conventional simulation because of the strongly nonlinear physics, such as multiphase flow and transport with oil/foam interactions. In this work, an operator-based linearization (OBL) approach, combined with the representation of foam by an implicit-texture (IT) model with two flow regimes, is extended for the simulation of the foam EOR process. The OBL approach improves the efficiency of the highly nonlinear foam-simulation problem by transforming the discretized nonlinear conservation equations into a quasilinear form using state-dependent operators. The state-dependent operators are approximated by discrete representation on a uniform mesh in parameter space. The numerical-simulation results are validated by using three-phase fractional-flow theory for foam/oil flow. Starting with an initial guess depending on the fitting of steady-state experimental data with oil, the OBL foam model is regressed to experimental observations using a gradient-optimization technique. A series of numerical validation studies is performed to investigate the accuracy of the proposed approach. The numerical model shows good agreement with analytical solutions at different conditions and with different foam parameters. With finer grids, the resolution of the simulation is better, but at the cost of more expensive computations. The foam-quality scan is accurately fitted to steady-state experimental data, except in the low-quality regime. In this regime, the used IT foam model cannot capture the upward-tilting pressure gradient (or apparent viscosity) contours. 1D and 3D simulation results clearly demonstrate two stages of foam propagation from inlet to outlet, as seen in the computed-tomography (CT) coreflood experiments: weak foam displaces most of the oil, followed by a propagation of stronger foam at lower oil saturation. OBL is a direct method to reduce nonlinearity in complex physical problems, which can significantly improve computational performance. Taking its accuracy and efficiency into account, the data-driven OBL-based approach could serve as a platform for efficient numerical upscaling to field-scale applications.

Introduction

Foam, discontinuous gas bubbles separated by liquid films, can improve the injection profile in gas-injection processes by reducing or mitigating the effects of high gas mobility and reservoir heterogeneity (Bikerman 1973; Schramm 1994; Rossen 1996; Dholkawala et al. 2007). Currently, foam is widely used in gas EOR, well-stimulation, and soil-remediation processes (Deshpande et al. 1999; Rossen and Wang 1999; Lake et al. 2014). Recently, the foam EOR technique is being extended to carbon dioxide storage, thus reducing greenhouse-gas emissions (Vitoonkijvanich et al. 2015; Izadi and Kam 2018; Rognmo et al. 2018; Esene et al. 2019). In these processes, foams mainly exhibit two steady-state flow regimes according to foam quality f_g (injected gas volume fraction): the high-quality and the low-quality regime, as illustrated in **Fig. 1** (Osterloh and Jante 1992; Alverez et al. 1999). These two regimes are essential to our understanding of foam, especially in the presence of oil. Because of the limited data available on foam/oil interaction, studies extending the model to oil are relatively few (Farajzadeh et al. 2012; Tang et al. 2018; Chen et al. 2018). This issue hinders the reliable design of foam processes.
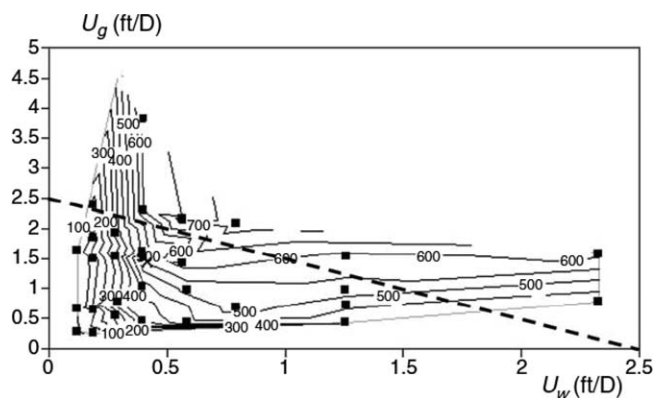

Fig. 1—Relationship between pressure gradient (in psi/ft) and superficial velocities (in ft/D) of water (U_w) and gas (U_g) at steady state, from Alverez et al. (1999). The dotted line represents a salinity scan at fixed total superficial velocity.

Some researchers have conducted laboratory experiments or field pilots to understand the complicated foam rheology and the mechanics of foam EOR with the presence of oil in porous media. Mannhardt et al. (1998) found that oil can kill foam completely after the oil saturation is greater than a critical oil saturation. This critical oil saturation represents the effect of oil on foam at local equilibrium (CMG 2012). This saturation is dependent on the type of oil, rock, and surfactant chemistry. However, there is not a broad range of experimental data to prove this theory in this literature. Some studies (Zanganeh et al. 2011; Andrianov et al. 2012; Osei-Bonsu et al. 2017; Zhang et al. 2020) investigated the oil effect on foam and found that most oils reduce foam stability, but did not provide a quantitative predictive model for the effect of oil.

Although there are numerous laboratory studies and field pilots on foam properties, numerical simulations of foam rheology and flow are relatively few, especially in the presence of oil in a porous medium, because of the challenges of accurate simulation and numerical issues. Hussain et al. (2017) found a single-cycle surfactant-alternating-gas flood can result in two different regions in a 3D case where the mobile oil is present (that is, foam overriding oil and gas overriding the foam). However, so far, there is no experimental evidence to prove their simulation results. Hosseini-Nasab et al. (2018) investigated the applications of the IT foam model for simulating foam flow in the presence of an oleic phase through the PumaFlow® (IFP, Rueil-Malmaison, France) reservoir simulator. The 1D model, however, causes some discrepancies between the measured and numerically calculated oil-recovery data. To design miscible carbon dioxide/foam flooding in a field trial, Alcorn et al. (2019) presented an integrated upscaling approach using the East Seminole Field and provided an improvement to the overall carbon dioxide/foam field pilot project design. However, the underlying mechanism of the oil effect on foam strength is not a focus of their work because the foam-quality scan is performed on water-saturated cores.

Currently, two fundamental approaches—population-balance models and local-equilibrium IT models—are used to represent the effect of foam on gas mobility. The population-balance models introduce a separate variable, lamella density, which describes the number of lamellae in one unit volume of the gas phase, in a new balance equation coupled with mass-conservation equations for each phase present in the porous medium (Falls et al. 1988; Friedmann et al. 1991; Kovscek et al. 1995; Rossen 1996; Kam et al. 2007). The local lamella density is obtained through solving this additional partial-differential equation at each location and timestep. The local-equilibrium implicit-texture modeling assumes foam generation and destruction reaches a local steady-state instantaneously (Marfoe et al. 1987; Islam and Ali 1988; Patzek and Myhill 1989; Fisher et al. 1990; Law et al. 1992; Cheng et al. 2000). A mobility-reduction factor, used to rescale gas mobility with foam, is introduced to implicitly represent the effect of gas bubbles. This mobility-reduction factor is a function of water saturation, oil saturation, surfactant concentration, capillary number, and salinity. These two models introduce nonlinear properties, especially when the oil is taken into account, which could increase the computational cost significantly. Moreover, foam behavior is complex, responding in an abrupt, nonlinear way to the variations of some properties, which might cause fluxes to fluctuate in time and space in simulations (Rossen 2013). Population-balance models are essential for representing the entrance regions of the core or formation where foam is created, the dynamics of foam propagation at the leading edge of the foam bank, and cases where foam generation is in doubt (Kovscek et al. 1995). They are much more complex than IT models, however, and must contend with the orders-of-magnitude difference in time scales of foam dynamics and displacement (Kam et al. 2007). Therefore, we use an IT model here.

To accurately simulate these highly nonlinear foam EOR processes, a finer computational grid in space or time can be implemented which, in turn, is counterbalanced by the increased simulation cost. At the field scale, because of the complexity and uncertainties of foam EOR processes, the computational cost is expensive to develop confidence in the prediction of field performance (Bascialla et al. 2017; Alcorn et al. 2020; Katiyar et al. 2020). Voskov (2017) proposed the new approach of OBL, where computational performance, flexibility, and robustness can be combined to improve the simulation performance of complex physical problems. The OBL approach transforms the discretized nonlinear conservation equations into a quasilinear form by means of grouping all variables defined by the physical state into state-dependent operators, which improves the simulation efficiency of the highly nonlinear physical problems. These state-dependent operators, relying on current local physical properties (e.g., relative permeability, viscosity, density), are approximated by discrete representation on a uniform or nonuniform mesh in parameter space (Khait and Voskov 2017; Khait et al. 2018). A multilinear interpolation is used to achieve the continuous representation of state-dependent operators, which provides an approximate representation of the exact physics of the physical problem with controlled error. This new approach also provides an opportunity to control the nonlinearity in physics by changing the resolution of parameter space (Khait and Voskov 2018).

In simulations, the resolution of the parameter space is one key factor that affects the accuracy of the OBL approach. To choose a proper resolution, a sensitivity study is required. A coarser parameterization space, corresponding to a smaller OBL resolution, can provide satisfying results, with higher efficiency compared with some academic or legacy simulators in previous tests (Khait and Voskov 2018; Kala and Voskov 2020; Wang et al. 2020). The proper implementation of the OBL approach can speed up Jacobian assembly by a factor of 14 and even faster on a graphics processing unit architecture (Khait et al. 2020), which saves computational costs significantly. To improve the accuracy, a higher OBL resolution can be always applied considering the efficiency of the new linearization scheme.

In this work, our aim is to investigate foam flow in porous media using an IT foam model in the presence of oil. The OBL approach is applied to improve the performance of numerical simulation. The Delft Advanced Research Terra Simulator, which is capable of modeling complex flow and transport related to various energy applications (Khait and Voskov 2018; Kala and Voskov 2020; Wang et al. 2020), is used to perform all simulation cases. First, the wet-foam model, as shown in Appendix A, is examined, where oil changes only the mobility of full-strength foam in the low-quality regime and has no direct effect on the high-quality regime. Then, the numerical-simulation results are validated using three-phase fractional-flow theory for foam/oil flow and we investigate the effects of grid resolution on the results. Next, we successfully obtain the parameters of the wet-foam model by fitting a single foam-quality scan using a least-squares optimization approach. Based on the fitting of steady-state experimental data with oil, numerical simulations are conducted to fit to foam-displacement experiments through our simulations by a gradient-optimization approach, assuming a 1D homogeneous model for the porous medium. Finally, using CT images, we construct a more accurate 3D heterogeneous model to represent the core used in the experiment. This high-fidelity 3D model is used to reproduce the displacement experiments. The developed simulator shows good performance with improved accuracy and flexibility.

Numerical Model

The governing equations and nonlinear formulation for three-phase three-component isothermal immiscible foam simulation are defined as

$$\frac{\partial}{\partial t}\left(\phi\sum_{j=1}^{n_p} x_{cj}\rho_j s_j\right) + \text{div}\sum_{j=1}^{n_p} x_{cj}\rho_j \mathbf{u}_j + \sum_{j=1}^{n_j} x_{cj}\rho_j \tilde{q}_j = 0, \quad c = 1, 2, ..., n_c, \quad \dots\dots\dots\dots (1)$$

where subscript $j \in \{g, o, w\}$ denotes phases present in the simulation. ϕ is porosity, s_j is phase saturation, ρ_j is phase molar density, x_{cj} is the component mole fraction in a phase, and $\mathbf{u}$ is Darcy velocity.

In addition, Darcy's law is applied to describe the flow of each phase,

$$\mathbf{u}_j = -k \frac{k_{rj}}{\mu_j}(\nabla p_j - \rho_j g \nabla D), \quad\quad\quad\quad\quad\quad\quad\quad\quad\quad\quad\quad (2)$$

where k and k_{rj} are permeability tensor and relative permeability, respectively. μ_j is phase viscosity, p_j is pressure in phase j, g is the gravitational acceleration, and D is the depth. The saturation constraint requires

$$\sum_{j=1}^{n_p} s_j = 1, \quad\quad\quad\quad\quad\quad\quad\quad\quad\quad\quad\quad\quad\quad\quad\quad\quad\quad (3)$$

where $s_j = \dfrac{v_j/\rho_j}{\sum_{j=1}^{n_j} v_j/\rho_j}$ and v_j is the molar fraction of phase j.

Nearly all foam models assume that foam has no direct effect on liquid properties (i.e., liquid properties do not change in the presence of foam). Instead, foam alters only the transport properties of the gas phase. These assumptions are in accordance with laboratory investigations (Friedmann et al. 1991; Rossen 1996; Dholkawala et al. 2007; Lotfollahi et al. 2016). Some gas is trapped by stationary lamellae to reduce gas mobility in the presence of foam. In the IT foam model (CMG 2012) studied here, a mobility-reduction factor (FM) is used to modify gas relative permeability in the presence of foam,

$$k_{rg}^f = k_{rg} \times \text{FM}, \quad\quad\quad\quad\quad\quad\quad\quad\quad\quad\quad\quad\quad\quad\quad\quad (4)$$

$$\text{FM} = \frac{1}{1 + fmmob \times F_1 \times F_2 \times F_3 \times F_4 \times F_5 \times F_6}, \quad\quad\quad\quad\quad (5)$$

where k_{rg}^f and k_{rg} are gas relative permeability in the presence and absence of foam, respectively; $fmmob$ is the maximum-attainable gas-mobility reduction (reference value); and F_1 through F_6 are functions that are used to account for the effects of different physical factors on gas mobility reduction (e.g., water saturation, surfactant concentration, capillary number, oil saturation, and salinity). In this project, only three functions, F_2, F_3, and F_5, are considered to capture the effects of water saturation, oil saturation, and shear thinning, respectively, in the low-quality regime.

The discretized mass-conservation equations based on a finite-volume method in space and backward Euler approximation in time are defined as

$$V\left[\left(\phi\sum_{j=1}^{n_p} x_{cj}\rho_j s_j\right)^{n+1} - \left(\phi\sum_{j=1}^{n_p} x_{cj}\rho_j s_j\right)^{n}\right] - \Delta t\sum_{l}\sum_{j=1}^{n_p} x_{cj}^l\rho_j^l\Gamma_j^l\Phi^l + \Delta t\sum_{j=1}^{n_p} x_{cj}\rho_j q_j = 0, \quad\quad\quad (6)$$

where $\Gamma_j^l = \Gamma^l k_{rj}^l/\mu_j^l$ is a phase j transmissibility over interface l, and Γ^l is the constant geometrical part of transmissibility. Φ^l is the pressure difference between neighbor cells. A two-point flux approximation in space and a fully implicit method in time are implemented to approximate Eq. 1. This approximation introduces strong nonlinearity into the system of governing equations. We use the overall composition of the mixtures and pressure as the primary unknown variables in our simulation. Then we linearize the problem, which requires determining all the partial derivatives with respect to these nonlinear unknowns and assembling the Jacobian and residuals. After the linearization step, the linearized system of equations is solved by the Newton-Raphson method on each nonlinear iteration,

$$J(\omega^k)(\omega^{k+1} - \omega^k) = -r(\omega^k), \quad\quad\quad\quad\quad\quad\quad\quad\quad\quad\quad\quad (7)$$

where $J(\omega^k)$ and $r(\omega^k)$ are the Jacobian and residual defined at the nonlinear iteration k, respectively, and ω is the set of primary unknown variables. In conventional simulation, the Jacobian should be assembled with accurate numerical property values and corresponding derivatives with respect to nonlinear unknowns, which is an expensive process.

OBL Approach

In this section, we introduce the framework of the OBL approach, which can reduce the number of nonlinear iterations needed to solve a complex physical problem. Then this new approach is validated by comparison between OBL solutions and analytical solutions. Three-phase fractional-flow theory and the wave-curve method are applied to find the analytical solutions (Castañeda et al. 2016; Tang et al. 2018).

Transformation of Governing Equations. Following the OBL approach, we combine the product of all properties in Eq. 1 that depend only on the thermodynamic state of the system (e.g., density, relative permeabilities) into state-dependent operators (Khait and Voskov 2017; Voskov 2017). The discretized mass-conservation equation is converted into operator form, given by

$$V\phi_0[\alpha_c(\omega) - \alpha_c(\omega_n)] + \sum_{l\in L(i)} \Delta t\Gamma^l\Phi_p^l\beta_c(\omega) + \theta(\omega, u) = 0, \quad\quad\quad\quad (8)$$

where

$$\alpha_c(\omega) = [1 + c_r(p - p_{\text{ref}})]\sum_{j=1}^{n_p} x_{cj}\rho_j s_j, \quad\quad\quad\quad\quad\quad\quad\quad\quad\quad (9)$$

$$\beta_c(\omega) = \sum_{j=1}^{n_p} x_{cj}\rho_j k_{rj}/\mu_j, \quad\quad\quad\quad\quad\quad\quad\quad\quad\quad\quad\quad\quad (10)$$

$$\theta(\omega, u) = \Delta t\sum_{j=1}^{n_p} x_{cj}\rho_j q_j(\omega, u), \quad\quad\quad\quad\quad\quad\quad\quad\quad\quad\quad (11)$$

where ω and ω_n are nonlinear unknowns in the current and previous timestep, respectively; $L(i)$ is the set of neighbors of the control volume l; and $\theta(\omega, u)$ is the source term. For simplicity, in our problem, the effects of gravity and capillarity are neglected, which means the phase potential differences are equal across all phases at any interface ($\Phi_{p,ij} = p_i - p_j$). In the presence of foam, the gas-flux operator should be rescaled by Eq. 4.

This representation allows us to significantly simplify the complicated numerical implementation of the simulation framework. The state-dependent operators are parameterized in physical space either at the preprocessing stage or by adaptively computing and storing the required supporting points in a simulation (Khait and Voskov 2018). The complex evaluations of properties and their derivatives with respect to nonlinear unknowns are completed by interpolating the operators in the current timestep with a multilinear interpolation. This process improves the performance of the linearization stage. Meanwhile, this approach can reduce the nonlinearity of the physical problem because of the application of piecewise representation of operators (Khait and Voskov 2017).

In Eq. 4, foams change only gas relative permeability. We schematically illustrate an example of gas-component operators parameterized at $N = 100$ (the supporting points in parameter space) for a binary compositional system, as shown in **Fig. 2,** to show how the OBL approach reduces the nonlinearity. Here, α_g and β_g correspond to the accumulation and flux terms of gas component in the mass-conservation equation, and p and z_w are pressure and the overall molar composition of one component (i.e., primary unknown variables). A multicomponent (n) isothermal system results in a set of supporting points in n-dimensional space. They are highly nonlinear in pressure/composition parameter space, especially given the sharp change of gas flux in the presence of foam. The sharp change in the flux term can make the nonlinear solver struggle to find the solution, but the OBL approach can smooth the sharp changes with sufficient accuracy, as shown in the following subsections. Meanwhile, this approach provides an opportunity to control the nonlinearity in physics by altering the operator space (that is, with a higher OBL resolution, the discretized physics is much closer to the real physics).

(a) Accumulation operator
(b) Flux operator
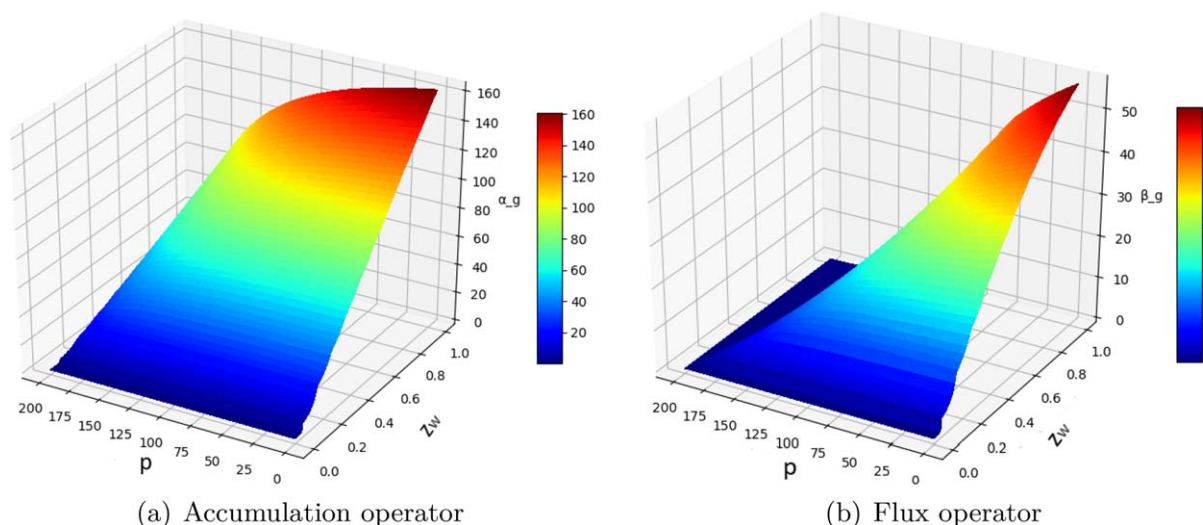
Fig. 2—Accumulation (Eq. 9) and flux operators (Eq. 10) of the gas component in a compositional system (immiscible) parameterized at $N = 100$. p and z_w are pressure and overall molar composition of the water component (i.e., primary unknown variables).

Validation of the Numerical Approach. In this part, the foam/oil-flow problem is solved by three-phase fractional-flow theory (Tang 2019), and we validate the numerical-simulation results by comparison with analytical solutions. The saturations of injection conditions (J) and initial conditions (I) in all cases presented are summarized in **Table 1.** All saturations listed here are normalized by Eq. 12 with respect to the total movable saturations, as in Tang (2019), except for the foam/oil parameters. On the basis of different J and I, we divide all these cases into four representative scenarios, with subscripts fm and nf denoting conditions inside or outside the foam region, respectively. Other parameters, such as relative permeability and dry-out parameters, used in these cases are given in Appendix A. In these cases, shear thinning is neglected to keep the same conditions as in the analytical solutions, and we assume that surfactant is already present in the water phase throughout the porous medium.

| Scenarios		Injection Conditions, $J = (S_w, S_o)$	Initial Conditions, $I = (S_w, S_o)$	Foam-Model Parameters, Scenario 1 (J_{nf} to I_{nf})
Scenario 1 (J_{nf} to I_{nf})	Case 1	$J = (0.2, 0)$	$I = (0.1875, 0.8125)$	$fmoil = 0.3$, $floil = 0.1$
Scenario 2 (J_{nf} to I_{fm})	Case 1	$J = (0.2, 0)$	$I = (0.7750, 0.2250)$	$fmoil = 0.3$, $floil = 0.1$
Scenario 3 (J_{fm} to I_{fm})	Case 1	$J = (0.3125, 0)$	$I = (0.7750, 0.2250)$	$fmoil = 0.3$, $floil = 0.1$
	Case 2	$J = (0.3125, 0)$	$I = (0.7750, 0.2250)$	$fmoil = 0.5$, $floil = 0.1$
Scenario 4 (J_{fm} to I_{nf})	Case 1	$J = (0.3125, 0)$	$I = (0.1875, 0.8125)$	$fmoil = 0.3$, $floil = 0.1$
	Case 2	$J = (0.3125, 0)$	$I = (0.1875, 0.8125)$	$fmoil = 0.5$, $floil = 0.1$

Table 1—A summary of cases presented for comparison between numerical and analytical solutions.

In Table 1, Case 1 refers to the reference cases to show the displacement structure, while Case 2 of Scenarios 3 and 4 with a higher *fmoil* are solved to illustrate foam stability at the foam-bank front and within an oil bank, respectively. These two cases allow foam injection but with different initial conditions. Normalized saturations are used in the Figs. 3 through 9,

$$S_j = \frac{S_{j,a} - S_{j,r}}{1 - S_{wc} - S_{or} - S_{gr}}, \quad \dots\dots\dots\dots\dots\dots\dots\dots\dots\dots\dots\dots\dots\dots\dots\dots\dots\dots\dots\dots\dots\dots\dots \quad (12)$$

where $S_{j,a}$ and $S_{j,r}$ are phase saturation and phase residual saturation, respectively. S_{or}, S_{wc}, and S_{gr} are residual oil saturation, connate water saturation, and residual gas saturation, respectively.

Figs. 3a through 6a illustrate the composition path in ternary composition space for Case 1 in four scenarios with $fmoil = 0.3$. In these four cases, the J and I are either inside or outside of the foam region. Because of the large value of $epdry$, F_6 in Appendix A, Eq. A-1 switches from 0 ($S_w < fmdry$) to 1 ($S_w > fmdry$) abruptly around $fmdry$. Hence, the mobility-reduction factor holds nearly constant for fixed oil saturation, although water and gas saturation vary. Figs. 3a and 4a describe the same injection condition, where S_w at J_{nf} is too low (too dry) to generate foam, although they have different initial conditions. S_o at I_{nf} is too high for foam to be stable, which causes the whole path to bypass the foam region (suggesting there is no foam generation at all) in Fig. 3a. Foam propagates some distance from the injection well in Fig. 4a, although its strength is substantially reduced by oil. Figs. 5a and 6a describe the same situation as the previous two cases except for altering J_{nf} to J_{fm}. As shown in Fig. 5a, where both J_{fm} and I_{fm} and the whole path are inside of the foam region, foam is generated starting from the injection well, and water saturation is sufficient to maintain foam. Meanwhile, oil does not kill foam entirely anywhere along the displacement. Nevertheless, most injected gas escapes ahead of the foam bank, which propagates very slowly. Fig. 6a shows the case where J_{fm} is inside but I_{nf} is outside of the foam region. The path crosses the foam boundary at $S_o = fmoil$ with a sharp inflection. Note that Case 1 in Scenario 2 presents a challenge to our simulations: The modeling results show oscillations as can be seen in Appendix B (Fig. B-1). By adding a small capillary-diffusion term, we eliminate the oscillations; see further details in Appendix B.

(a)   (b)
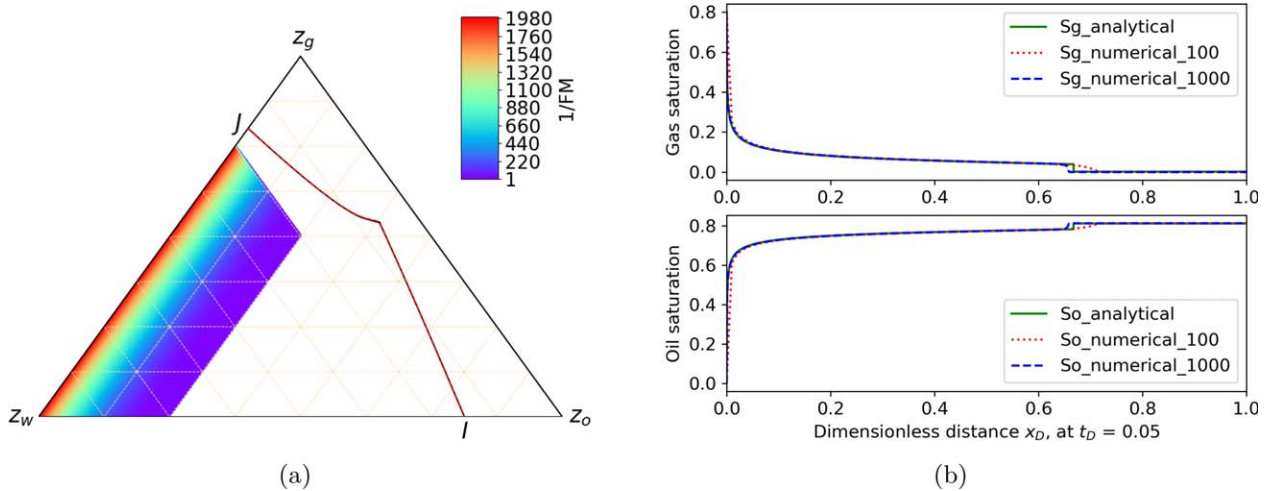
Fig. 3—(a) Composition path ($fmoil = 0.3$) for Case 1 of Scenario 1 in a ternary diagram. Both injection (J) and initial (I) conditions are outside the foam region. The three vertices represent the compositions of gas, oil, and water, respectively. The region with colors is the foam region, with color indicating magnitude of mobility reduction; the rest is the no-foam region. The black solid line is the analytical solution, and the red dashed line is the OBL solution in the ternary diagram. (b) Gas-saturation and oil-saturation profiles as a function of dimensionless position x_D at time $t_D = 0.05$ PVI. The 100 and 1,000 in the numerical solutions represent different grid resolutions.

(a)   (b)
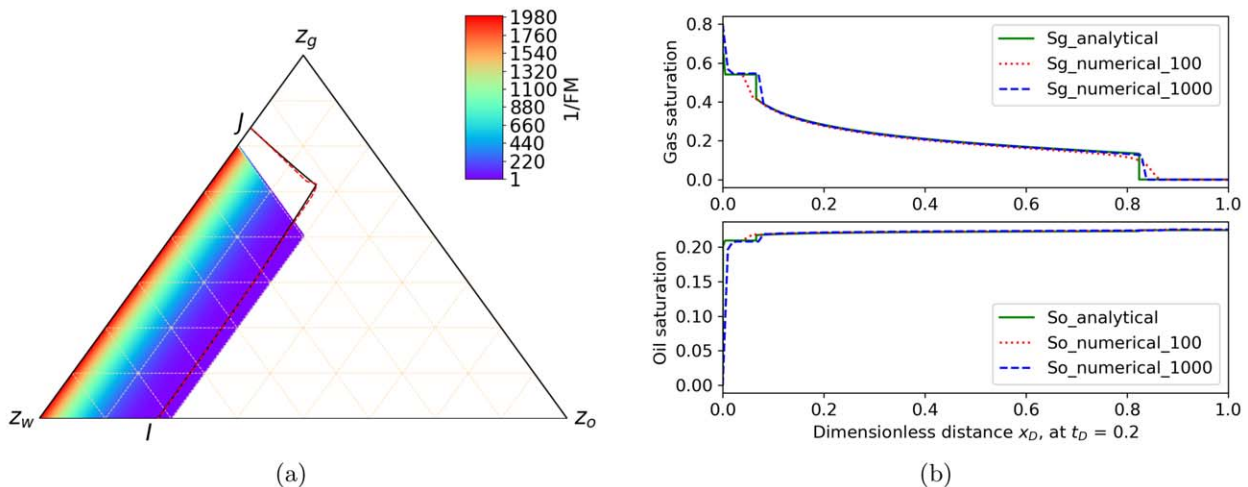
Fig. 4—(a) Composition path ($fmoil = 0.3$) for Case 1 of Scenario 2 in a ternary diagram. The injection condition (J) is outside, but the initial condition (I) is just inside the foam region. (b) Gas-saturation and oil-saturation profiles as a function of dimensionless position x_D at time $t_D = 0.2$ PVI. The 100 and 1,000 in the numerical solutions represent different grid resolutions.

Fig. 5—(a) Composition path (*fmoil* = 0.3) for Case 1 of Scenario 3 in a ternary diagram. Both injection (*J*) and initial (*I*) conditions are inside the foam region. (b) Gas-saturation and oil-saturation profiles as a function of dimensionless position x_D at time $t_D = 0.2$ PVI. The 100 and 1,000 in the numerical solutions represent different grid resolutions.
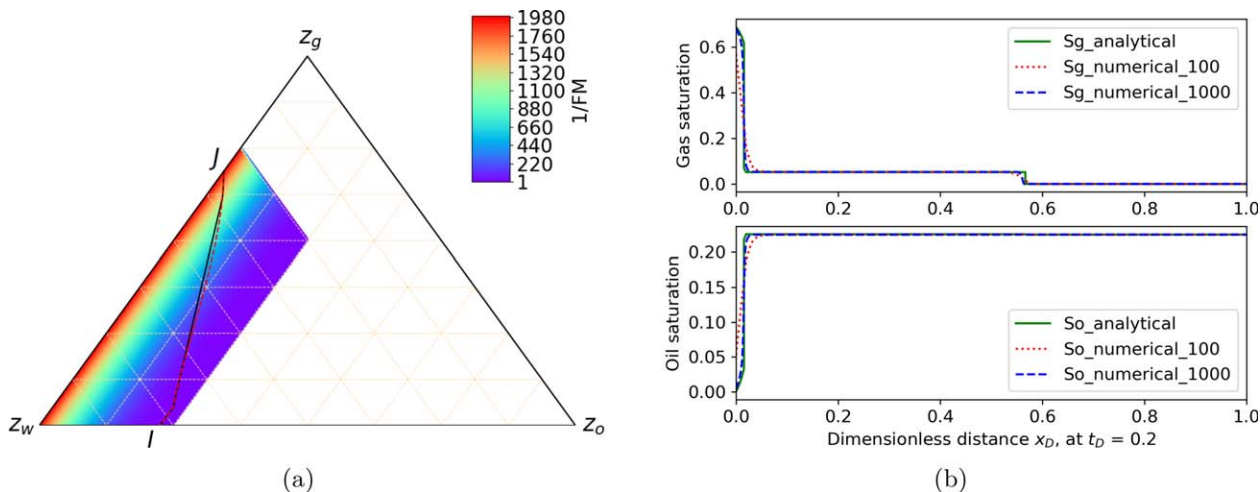

Fig. 6—(a) Composition path (*fmoil* = 0.3) for Case 1 of Scenario 4 in a ternary diagram. The injection condition (*J*) is inside, but the initial condition (*I*) is outside the foam region. (b) Gas-saturation and oil-saturation profiles as a function of dimensionless position x_D at time $t_D = 0.4$ PVI. The 100 and 1,000 in the numerical solutions represent different grid resolutions.
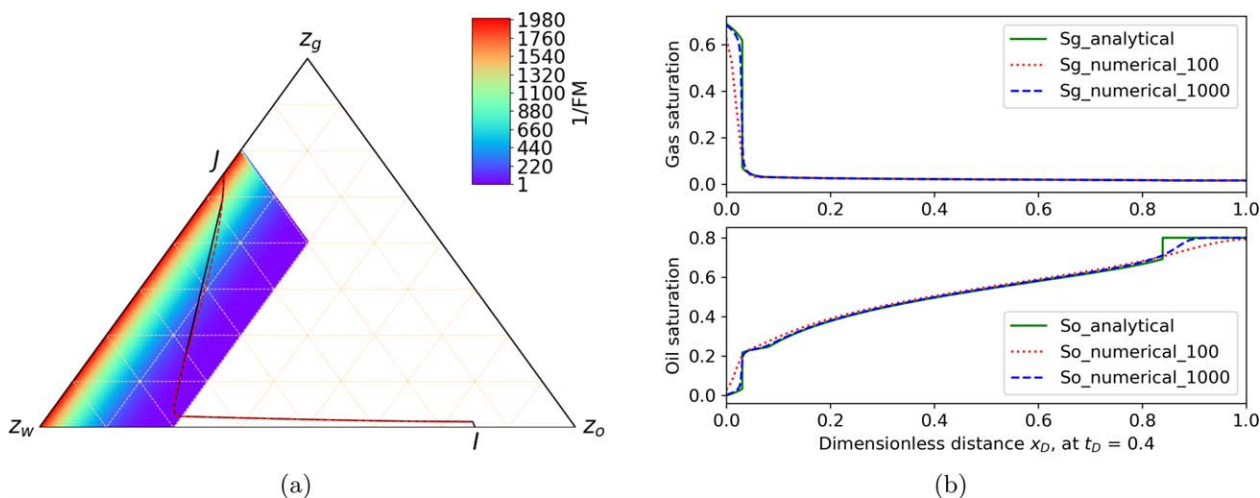
Figs. 3b through 6b illustrate the saturation profile at the given pore volume injected (PVI) for Case 1 in four scenarios with *fmoil* = 0.3. Comparing Fig. 3b, without foam, with Fig. 6b, gas is much more mobile than oil (and water), which causes extremely slow oil displacement. However, the slow-moving foam bank displaces nearly all oil, as shown in Fig. 6b. Ahead of the foam region, waterflooding reduces S_o below *fmoil* and allows a stable foam bank to form. In Fig. 4b, gas hardly displaces oil but can displace water forward. In Fig. 5b, the gas saturation is high near the entrance, suggesting that foam displaces oil there, although very slowly.

For Case 2 in Scenarios 3 and 4, a larger *fmoil* than that in Case 1, representing a surfactant formulation more tolerant to oil, is used to analyze the displacement. **Figs. 7 and 8** demonstrate that the increase in *fmoil* extends the foam region, reflecting foam more stable to oil. Fig. 7a illustrates that ahead of foam bank, an oil bank ($S_o > S_{o,i}$) is created, but S_o in the oil bank cannot exceed the upper limit *fmoil* for stable foam. Therefore, oil within the oil bank reduces foam strength but does not kill foam completely, which keeps the whole path inside the foam region. Fig. 8a exhibits the composition path for I_{nf} outside of the foam region, where the stable foam is not allowed, although the foam region is extended by increasing *fmoil*.

Figs. 3b through 8b also illustrate the influence of grid size on the prediction by the OBL approach. In all cases, the difference in saturation profiles shows that when using a finer grid, the numerical results are much closer to the analytical solution. The computational cost, however, increases. For example, it takes 0.478 seconds, with 3,117 Newton iterations, for a coarse mesh (100 gridblocks) by the end of simulation in Case 2 of Scenario 3. When using a finer mesh (1,000 gridblocks), it takes 5.41 seconds with 4,669 Newton iterations. As seen in Fig. 7b, simulation does not well-capture the shock at $x_D = 0.25$ to 0.30. The change of saturation along this shock is quite small: Gas saturation jumps from 0.401 to 0.362, which requires greater resolution of both the OBL and grid to reproduce the shock more accurately **(Fig. 9b).** Here, to save computational time, we do not use very fine OBL and grid resolutions for these comparisons. In our work, we do not present a detailed analysis of the displacement [i.e., the positions of the shocks and spreading waves, which have been demonstrated in Tang (2019)]. We mainly focus on the stability and accuracy of this new linearization approach. From these six cases, we can deduce that the OBL approach can capture the complex foam physical behavior and have overall good agreement with analytical solutions with acceptable accuracy.
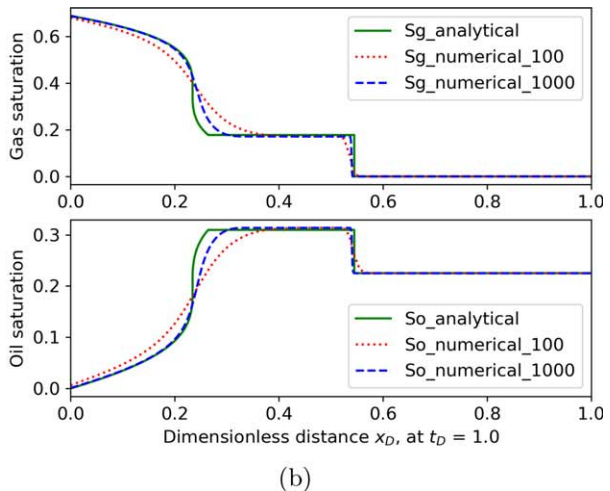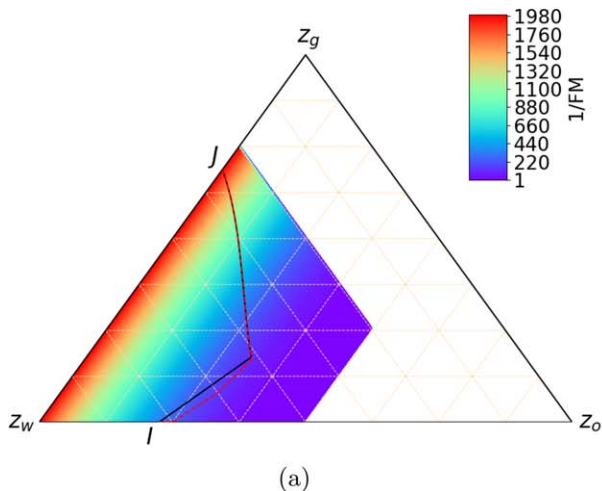
Fig. 7—(a) Composition path (*fmoil* = 0.5) for Case 2 of Scenario 3 in a ternary diagram, with injection (*J*) and initial (*I*) conditions both inside the foam region. In this case, *fmoil* is increased to 0.5. (b) Gas-saturation and oil-saturation profiles as a function of dimensionless position x_D at time t_D = 1.0 PVI. The 100 and 1,000 in the numerical solutions represent different grid resolutions.

Fig. 8—(a) Composition path (*fmoil* = 0.5) for Case 2 of Scenario 4 in a ternary diagram, with injection condition (*J*) inside but initial condition (*I*) outside the foam region. In this case, *fmoil* is increased to 0.5. (b) Gas-saturation and oil-saturation profiles as a function of dimensionless position x_D at time t_D = 0.25 PVI. The 100 and 1,000 in the numerical solutions represent different grid resolutions.

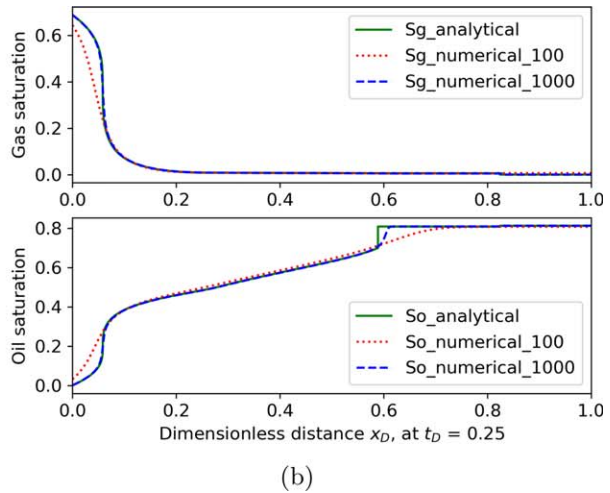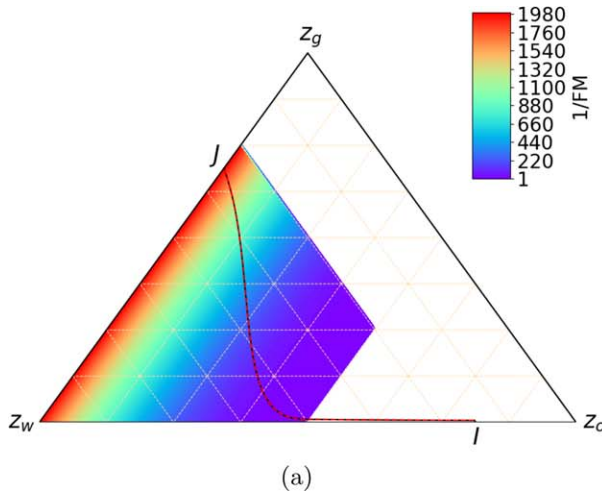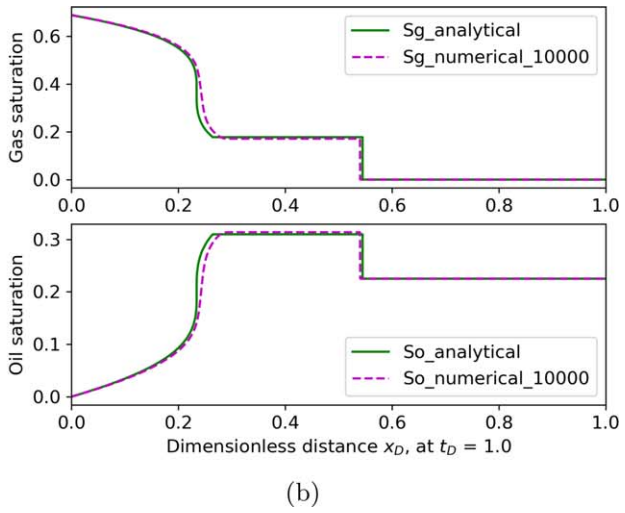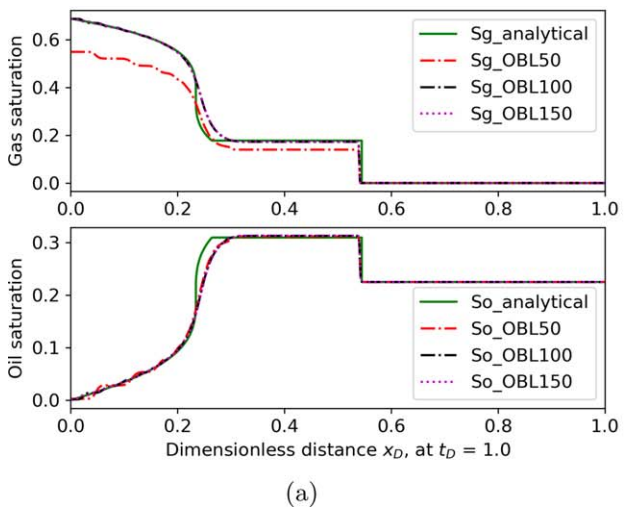**Fig. 9—Comparison between gas saturation (upper) and oil saturation (lower) for different resolutions of parametrization in Case 2 of Scenario 3. (a) Different OBL resolutions with 1,000 gridblocks; (b) fine-grid (10,000) and fine-OBL resolution (150).**

Effect of OBL Resolution. To demonstrate the effect of the OBL resolution, we show a set of simulations and compare the reference solution with results obtained at different resolutions using Scenario 3, Case 2 (Fig. 7b). In Fig. 9a, we present the spatial distribution of gas saturation and oil saturation at time $t_D = 1.0$ PVI for simulations with different OBL resolutions (i.e., different distances between supporting points in parameter space). From Fig. 9a, we can see the difference between the analytical solution and the parametrized solutions with three different resolutions of parameter space. The finest resolution shown in Fig. 9a contains 150 values for each unknown and it obtains good agreement with the analytical solution with acceptable accuracy. However, when the resolution is 50, there is a big difference between the analytical solution and the numerical solution, which indicates that a finer OBL resolution is required to capture the highly nonlinear foam physics. The results with the two higher resolutions are close to each other, which demonstrates that increasing OBL resolution can improve the numerical accuracy. However, the benefit is reduced at some point: if one resolution gives a good approximation, increasing resolution continuously cannot improve accuracy significantly. Moreover, a higher resolution increases the computational cost because it takes longer time to interpolate the solutions.

Fig. 9a shows that the two finer resolutions approach each other, but still smear out the shock at $x_D = 0.23$. This mismatch is caused by numerical dispersion. The first shock exits between the foam bank (behind the shock) and oil bank (ahead of the shock). As mentioned previously, the variation of saturation along this shock is quite small; thus, a finer resolution for both OBL and grid is required to reproduce the shock more accurately. As shown in Fig. 7b, a coarse grid gives a smooth change near the shock; however, the numerical solutions obtained from a finer mesh show better agreement with the analytical solutions (i.e., a sharp transition near the shock followed by a spreading wave). We can infer that with the decrease of gridblock size, the shock position can be reproduced within a small deviation (Nell 2015). A finer grid resolution can reduce the effect of numerical dispersion (Fig. 9b), but again, the computational cost also increases.

Foam Parameter Fitting and CT Coreflood Simulation

Foam Model Fit to Steady-State Data. Fitting foam scans to obtain foam parameters can be performed using several techniques. One technique, proposed by Boeije and Rossen (2015), can quickly provide an initial estimate of foam parameters. However, it assumes a large value of *epdry* (i.e., an abrupt transition between the low- and high-quality regimes). Zeng et al. (2016) proposed an algorithm to estimate foam parameters in the absence of oil using linear regression and single-variable optimization. To obtain the water-saturation-dependent and shear-rate-dependent parameters, two kinds of experiments are performed: foam-quality scan with fixed total superficial velocity and flow-rate scan with fixed foam-quality experiments. Zeng et al. (2016) assume that in quality-scan experiments, the shear-thinning effect can be ignored because the total flow rate was held constant. This is not true in the STARS™ (Computer Modelling Group, Calgary, Alberta, Canada) model (Boeije and Rossen 2015). The ability to fit oil-saturation dependence is also unclear. A third approach uses a nonlinear least-squares minimization, which can simultaneously compute all seven parameters by minimizing the sum of squared errors (Kapetas et al. 2015). The same foam-scan data can be fitted roughly equally well by using the Boeije and Rossen (2015) approach and a nonlinear least-squares minimization method (Kapetas et al. 2015). In our work, the latter approach is implemented to obtain the foam parameters by fitting the experimental data in the presence of oil.

Tang et al. (2018) performed steady-state foam experiments in the presence of oil. In their experiments, the surfactant concentration is 0.5 wt%, which is greater than the critical concentration. Oil was coinjected with foam at a fixed ratio of oil/water superficial velocity. Unfortunately, oil saturation was not measured in these experiments. We assume that Corey relative permeability functions can be applied to three-phase flow; then, oil saturation is obtained indirectly through flow and pressure data using Darcy's law. In this work, we fit only the experimental data with hexadecane (C_{16}), which is benign to foam stability, using the wet-foam algorithm, where oil changes the mobility of full-strength foam in the low-quality regime. The foam-simulation model includes the parameters *fmmob*, *fmdry*, *epdry*, *fmcap*, *epcap*, *fmoil*, *floil*, and *epoil*, while the fluid and transport properties used in the parameter fitting could be found in Tang et al. (2018). The detailed procedure is described as below:

- Step 1: Draw ∇p contours. One might need to screen the data and smooth the ∇p contours to efficiently fit foam parameters. For fixed ∇p, the fitted contour comprises a vertical line (the high-quality regime) and a horizontal line (the low-quality regime), as shown in Fig. 1.
- Step 2: Plot a single foam-quality scan. Pick one fixed total superficial velocity (U_t), and then one can determine ∇p along this scan by making a diagonal line.
- Step 3: Determine the oil saturation with respect to the corresponding water saturation. Without the effect of gravity and capillary pressure, Darcy's law is applied to the water phase to obtain the water saturation. Water relative permeability is thus obtained; then, oil relative permeability can also be obtained because of the fixed ratio of oil/water superficial velocity. Using Corey relative permeability, one can calculate the oil saturation.
- Step 4: Define the objective function. After water- and oil-phase saturations are known, one can define the objective function. In our project, foam apparent viscosity is implemented as the objective function,

$$\min f = \sum_{i}^{n} (\mu_{app_{exp}} - \mu_{app_{model}}), \quad\dots\dots\dots\dots\dots\dots\dots\dots\dots\dots\dots\dots\dots\dots\dots\dots\dots\dots\dots\dots\dots\dots\dots\dots (13)$$

$$\mu_{app_{model}} = \frac{1}{k_{rw}(S_w)/\mu_w + k_{rg}(S_w) \times \mathrm{FM}(S_w, S_o, \nabla p)/\mu_g + k_{ro}(S_w)/\mu_o}. \quad\dots\dots\dots\dots\dots (14)$$

- Step 5: Apply a nonlinear least-square minimization approach to find the optimal solution in the given range by minimizing the sum of squared errors.

Fig. 10 and **Table 2** show the final data fit for the foam-quality-scan experiment. In the high-quality regime, the model shows good agreement with experimental data. In our model, foam behaves as a Newtonian fluid, and oil does not change foam strength in the high-quality regime (Boeije and Rossen, 2015; Tang et al. 2019). Therefore, and because a large value of *epdry* fits the data, the fit gives a straight line in this regime. In the low-quality regime, although the effects of oil saturation, water saturation, and shear-thinning rheology on foam are taken into account, our model does not show perfect agreement with the experimental data, especially where foam quality approaches the transition between regimes.

After these foam parameters are obtained, the pressure-gradient/velocity contours are constructed. **Fig. 11** compares these contours with the experimental data. The model fit provides a good match with experimental data and the implemented wet-foam model can predict the foam behavior in high- and low-quality regimes. However, in the low-quality regime, this model cannot capture the upward-tilting ∇p contours and, therefore, ∇p in this regime is greatly overestimated at high water superficial velocity (Tang et al. 2018).

Pressure gradient increases with increasing water velocity in the low-quality regime in the experiments (see red contour in Fig. 11) (Kim et al. 2005): Pressure gradient is not independent of water velocity in the low-quality regime. To address this issue, this foam model should be improved to represent this behavior in the low-quality regime. This lies beyond the scope of this work.
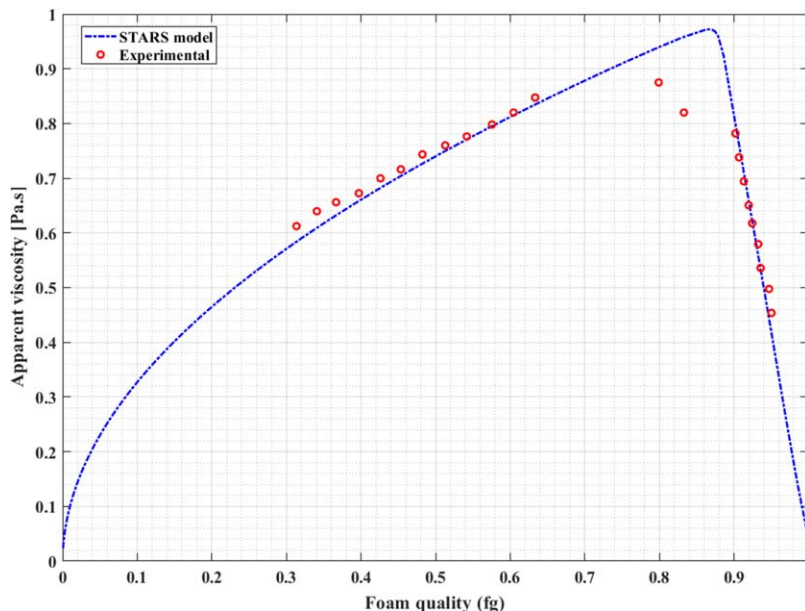

Fig. 10—Relationship between apparent viscosity and foam quality (f_g) at fixed U_t = 3 ft/D in a Bentheimer Sandstone core, from Tang et al. (2018).

Foam Parameters	Values	Foam Parameters	Values
fmmob	50,000	epcap	1.321
fmdry	0.215	fmoil	0.823
epdry	19,950	floil	0.295
fmcap	0.0001	epoil	3.827

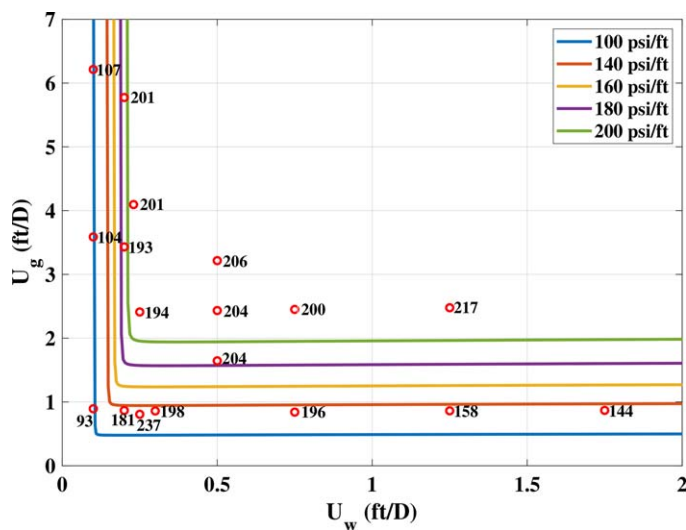Table 2—STARS model parameters fitted to the foam-scan experiment.

Fig. 11—Model fit by use of our method to the data of Tang et al. (2018). The numerical values are experimental data.

Simulation of CT Foam Coreflood with Oil. In this subsection, we model a CT coreflood study of foam displacement with C_{16} (Tang 2019). Our purpose is to understand the transient dynamics of foam using the OBL approach with the experimental data. We also want to check whether the foam parameters obtained at steady state can be applied to a foam-displacement process. The core sample in the experiment is Bentheimer Sandstone with length of 40 cm, diameter of 4.0 cm, porosity of 0.22, and absolute permeability of 2,820 md. The core is initially filled with water and oil (S_{oi} = 0.46 and S_{wi} = 0.54, respectively) and pregenerated foam is injected into the core with f_g = 70%. In the simulation, a simple 1D domain consisting of 100 grid cells is used to represent the core. An OBL resolution of 500 is chosen in this case, which is sufficient to represent underlying nonlinear physics. The foam parameters are taken from the steady-state experiments, as shown in Table 2.

Tang et al. (2018) did not measure the foam-free relative permeability functions for each phase in their CT coreflood experiments, which adds some uncertainties to the simulation. To match the experiment data accurately, we adopted a gradient-optimization technique to regress the relative permeability parameters according to the Corey model. The details and results are shown in Appendix C. Implementing these new parameter values (i.e., parameters of Corey relative permeability), we run the simulation for an experiment period. **Fig. 12** shows the phase-saturation profiles at different PVI values. The oil saturation in the oil bank in the experiment is approximately 0.8. From the steady-state foam modeling, the critical oil saturation *fmoil* is 0.827. A stable oil bank forms, with oil saturation lower than *fmoil* in the simulation, as in the experiment. Foam in forward propagation creates an oil bank with S_o of approximately 0.8 at the displacement front in the coreflood experiment (Fig. 12). S_g is roughly zero ahead of the foam front, as seen from gas-saturation profiles. This suggests that most gas is held within the foam bank.
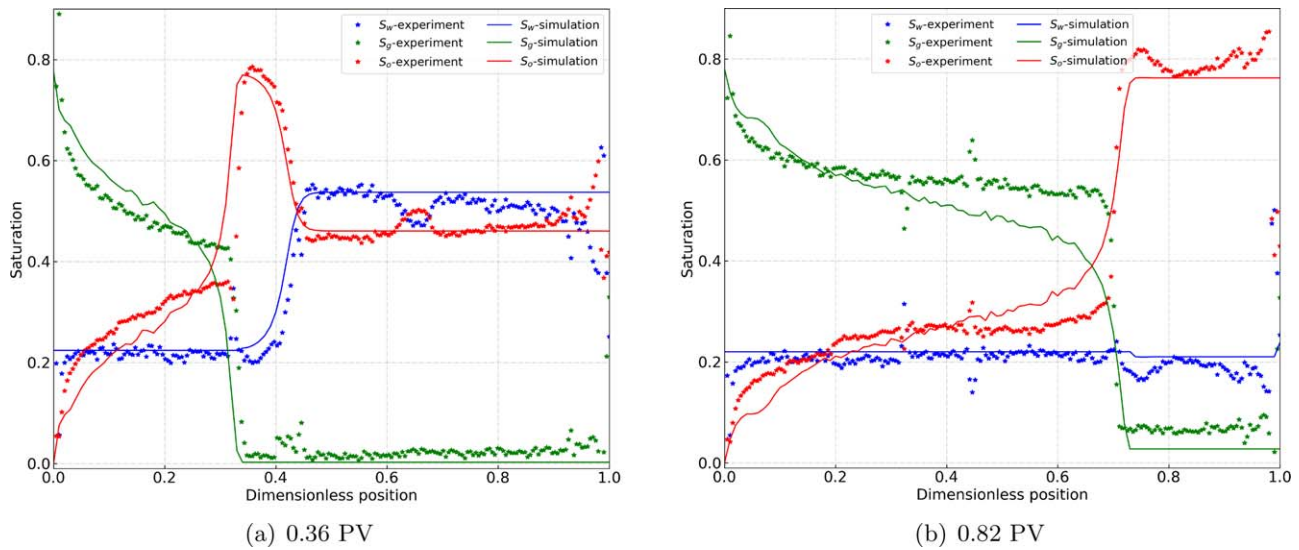

Fig. 12—Phase-saturation profiles vs. dimensionless position at different PVIs.

These results show that the OBL approach can be used to fit model parameters to foam-displacement coreflood data. Notice that with the relative permeabilities adjusted to fit the displacement coreflood data and the foam-model parameters fixed, the model no longer fits the steady-state data. The model fit overestimates mobility in the low-quality regime by approximately 15%. Moreover, the new relative permeability parameters place S_{wc} (0.197) so close to *fmdry* (0.215) that the high-quality regime virtually disappears from the fit. It is possible that fitting both steady-state and coreflood displacement data simultaneously could obtain a satisfactory fit to both. Or, it is possible that the model itself cannot represent the full physics of foam behavior. This issue remains for future investigation. However, the proposed approach helps in the representation of the physical phenomena identified during our foam experiments in realistic 3D numerical simulations.

3D CT Coreflood. To demonstrate the application of our approach, we build a 3D heterogeneous simulation grid using the CT images. To determine porosity in each pixel, we use the correlation (Sharma et al. 1997)

$$\phi = \frac{CT_{brine} - CT_{air}}{CT_w - CT_a}, \quad \dots\dots\dots\dots\dots\dots\dots\dots\dots\dots\dots\dots\dots\dots\dots\dots\dots\dots\dots\dots\dots\dots\dots\dots\dots\dots\dots\dots (15)$$

where CT_{brine} is CT attenuation of a fully brine-saturated core; CT_{air} is CT attenuation of a dry core; and CT_w and CT_a are CT attenuation of water and air, respectively. Such a correlation is applied to each CT slice (e.g., the gray circular area in **Fig. 13a**). Then the porosity of each triangular gridblock can be evaluated to obtain the porosity distribution, as shown in Figs. 13b and 13c. On each slice, an unstructured map with 1,080 elements is used to represent the porosity distribution, with an average cell area of 1.16 mm². From the CT scan, one can see that the variation of porosity in the Bentheimer core is relatively small.
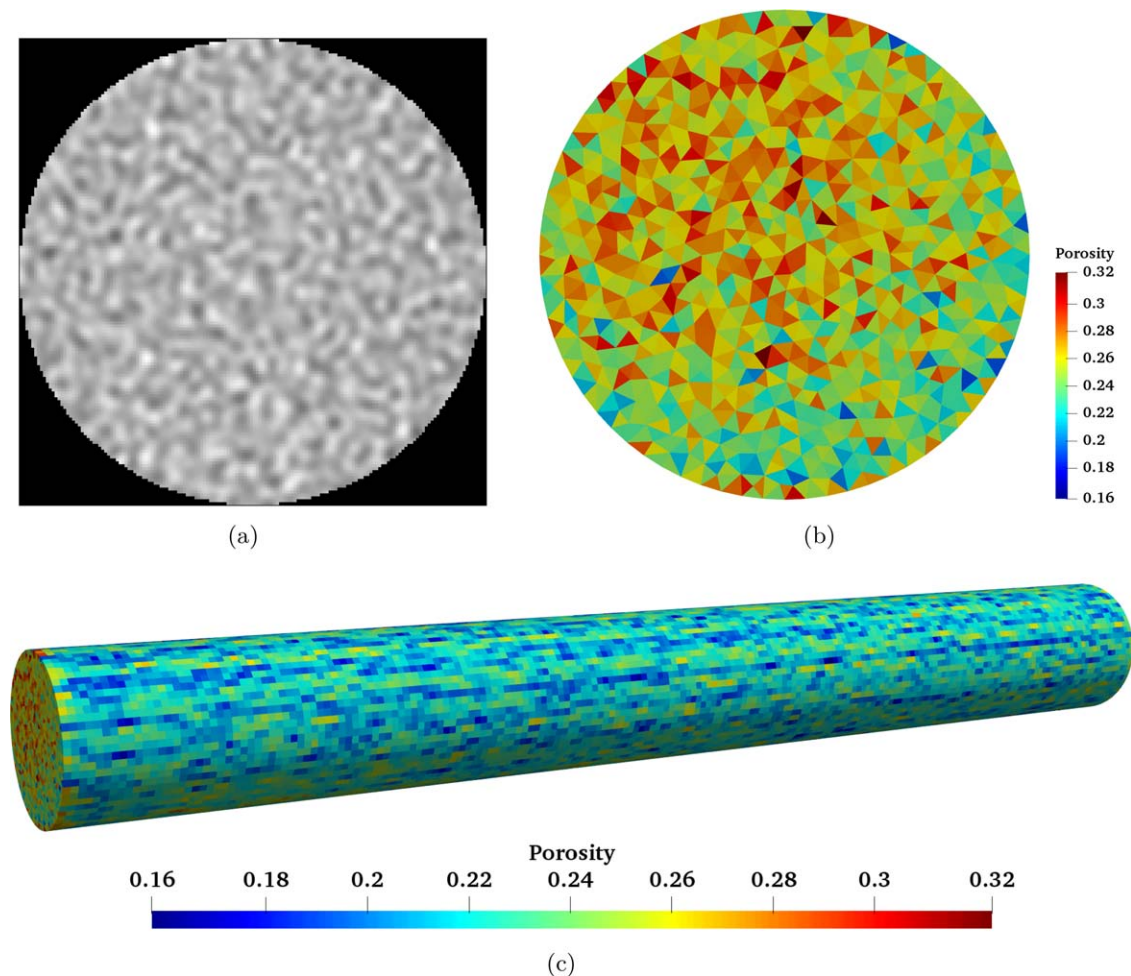
Fig. 14 shows the frequency histogram of the porosity data extracted from the CT images. For this Bentheimer Sandstone, the average porosity is approximately 0.23, which is consistent with the values in the literature where the porosity of Bentheimer Sandstone is reported (Kapetas et al. 2015; Eftekhari and Farajzadeh 2017; Tang et al. 2018). Then, according to the Kozeny-Carman equation (Chapuis and Aubertin 2003), the corresponding permeability is

$$k = \alpha \frac{\phi^3 D_p^2}{(1 - \phi)^2}, \quad \dots\dots\dots\dots\dots\dots\dots\dots\dots\dots\dots\dots\dots\dots\dots\dots\dots\dots\dots\dots\dots\dots\dots\dots\dots\dots\dots\dots\dots (16)$$

where k is the absolute permeability (in md), D_p is the average diameter of sand grains (in mm), ϕ is the porosity of the core plug, and α is the proportionality and unity factor (in md/mm²). Because of the limited experimental data, we assume that permeability has a same distribution as porosity (i.e., the mean permeability shares the same frequency as the mean porosity). With this assumption, once we know the average porosity and average permeability, a combination of α and D_p^2 can be obtained to calculate permeability distribution using the porosity distribution from the CT image.

After the porosity and permeability data are obtained, we run the model for 0.36 PVI using the same parameters as in the previous case (apart from allowing for heterogeneous porosity and permeability). In this work, we mainly focus on whether the OBL approach can capture the oil bank seen in the experiment, which cannot be accurately predicted by conventional physics using the steady-state

model. The distribution of phase saturations is shown in **Fig. 15.** Fig. 15a displays the gas-saturation distribution along the vertical plane on the central axis of the core. From the inlet to the gas front, a foam region is formed that displaces an oil bank ahead of it. However, the foam near the oil bank is weakened because of the increasing oil saturation. Ahead of the gas front, an oil bank with a higher oil saturation is created, which further reduces the foam strength (Fig. 15b). Our 3D simulation results show good overall agreement with CT coreflood results in terms of saturation profiles **(Fig. 16).** It is obvious that 3D simulation results more accurately represent the displacement regimes observed in the experiment compared with 1D simulation.

Fig. 13—Porosity profile of sandstone example: (a) CT image; (b) porosity profile; and (c) porosity distribution along the core.
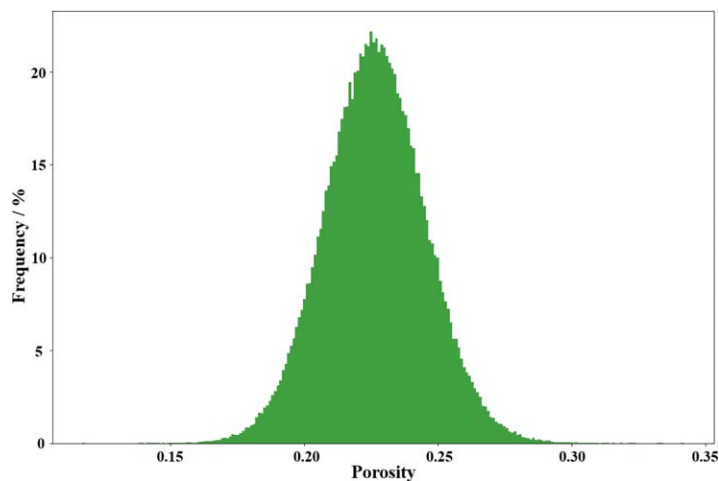
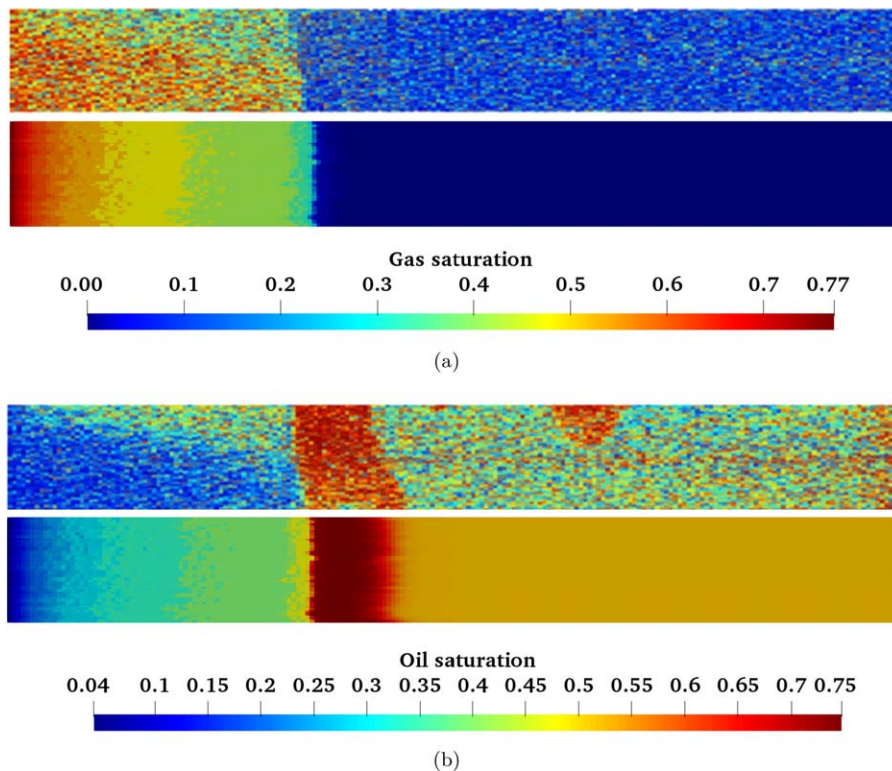**Fig. 14—Frequency histogram of the porosity data.**

Fig. 15—Gas-saturation and oil-saturation profiles at t_D = 0.36 PVI along the vertical plane at the central axis of the core. The top figure in (a) and (b) is the CT image, and the bottom is the simulation result.
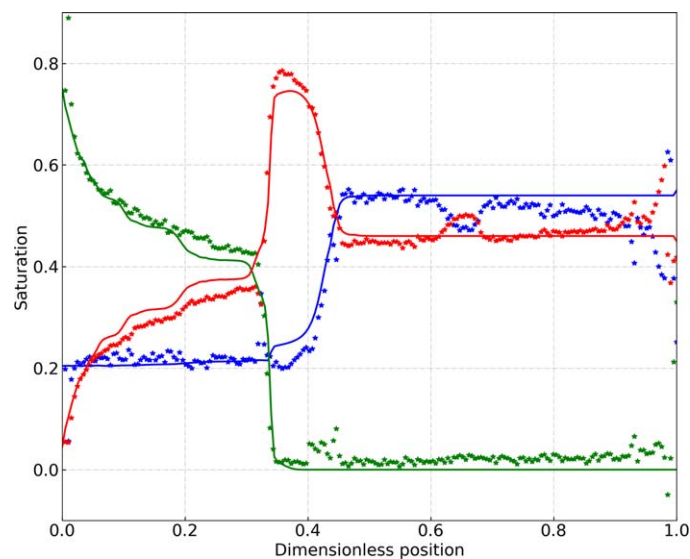

Fig. 16—Phase-saturation at t_D = 0.36 PVI. The average saturation of each slice along the core is plotted, along with the comparison with the experimental data.

Compared with the CT image in Fig. 15, there are still some small differences between the numerical results and the experimental results. The first is that oil saturation is greater at the top of the core behind the oil bank in the CT image. Although gravity is included in our simulation, this phenomenon is not fully resolved in the 3D model. The second is that there are some locations where oil saturation is slightly higher in the experiment compared with our simulation. Some further work is needed to explore the reasons causing these differences. However, the 3D coreflood simulation provides us with the following new insights to investigate the behavior of foam displacement compared with the 1D model:

- The heterogeneity of the core can be taken into account using the 3D simulation grid. Although the porosity of Bentheimer Sandstone used in this experiment shows a small variability, this heterogeneous grid is more realistic. More physics can then be included, such as capillary heterogeneity and gravity.
- Heterogeneity is an important factor that affects the foam strength (Kapetas et al. 2015; Al Ayesh et al. 2017). The 3D heterogeneous core can be used to investigate the effect of small-scale heterogeneity on foam EOR processes.

Our future work will focus on the development of the data-driven approach to include more physics to represent behavior exactly and on extending this approach to general-purpose reservoir-simulation problems, such as a field-scale pilot. In addition, we will

develop an extension of this approach to systems with gravity- and capillary-dominated flow, which have a great effect on foam behavior. These systems introduce many nonlinearities to challenge Newton-based nonlinear solvers. A more robust nonlinear strategy is required to efficiently and accurately solve these models with highly nonlinear physics.

Conclusions

In this work, we extend a new linearization technique, OBL, to foam-related simulation. The benefit of this nonlinear strategy is that the potential problem introduced by the rapid property-gradient changes in the presence of foam with oil can be resolved successfully with greater performance.

We compare our linearization approach with analytical solutions according to fractional-flow theory. The OBL approach shows good agreement with the analytical solutions except in the case where the initial oil saturation is close to *fmoil*. To avoid oscillations in saturation profiles, a capillary-diffusion term, which eliminates the oscillations, is introduced. Note that this correction is only required for nearly numerical dispersion-free simulations performed for an accurate representation of the analytic solution. The nonlinear least-squares minimization approach can give a good match with the foam-scan data, but still cannot capture the upward-tilting ∇p contours in the low-quality regime because of a limitation of the current foam model.

Given the foam parameters obtained from steady-state experiments, it is still a challenge to match the experimental data. The gradient-optimization technique improves the accuracy of simulation significantly by optimizing the relative-permeability data. However, according to the fitted parameters, the 1D simulation does not show a perfect match with experimental results because of the limitation of the steady-state foam model. The 3D simulation results improve the accuracy but still miss a few important features. It might be important to explore a new model, such as the population-balance model, to accurately represent the dynamic behavior of foam in porous media.

We introduce the OBL approach here and illustrate its accuracy and usefulness in simulations of laboratory-scale experiments. There are additional challenges involved in scaling up simulations for reservoir applications, among them representing the range of conditions (temperature, salinity, surfactant concentration, formation properties) that would be encountered in a reservoir application, surfactant retention in the formation, modeling the effects of heterogeneities below the gridblock scale, the effects of layer boundaries on foam properties (Shah et al. 2020), and near-well mechanisms affecting foam injectivity (Gong et al. 2020). Incorporating these factors into field-scale simulation remains a research priority.

Nomenclature

$$
\begin{aligned}
c_r &= \text{rock compressibility, 1/bar} \\
CT_a &= \text{CT attenuation of air} \\
CT_{air} &= \text{CT attenuation of dry core} \\
CT_{brine} &= \text{CT attenuation of fully brine-saturated core} \\
CT_w &= \text{CT attenuation of water} \\
D &= \text{vertical depth vector (up-down oriented), m} \\
D_p &= \text{average diameter of sand grains, m} \\
epcap &= \text{exponent for shear thinning effect} \\
epdry &= \text{parameter controlling the abruptness of foam collapse} \\
epoil &= \text{exponent for oil effect} \\
floil &= \text{lower-limiting oil saturation} \\
fmcap &= \text{reference capillary number} \\
fmdry &= \text{limiting water saturation} \\
fmmob &= \text{maximum-attainable gas-mobility reduction} \\
fmoil &= \text{upper-limiting oil saturation} \\
FM &= \text{mobility reduction factor} \\
F_1 \text{ through } F_6 &= \text{different physical factors on gas mobility reduction} \\
F_2 &= \text{effect of water saturation} \\
F_3 &= \text{effect of oil saturation} \\
F_5 &= \text{effect of shear thinning} \\
N_{ca} &= \text{capillary number} \\
J &= \text{Jacobian} \\
k_{rg} &= \text{gas relative permeability in the absence of foam} \\
k_{rg}^f &= \text{gas relative permeability in the presence of foam} \\
k_{rj} &= \text{phase relative permeability} \\
k_{ro} &= \text{oil relative permeability} \\
k_{rw} &= \text{water relative permeability} \\
K &= \text{effective permeability tensor, md} \\
n_c &= \text{number of components} \\
n_i &= \text{exponent for phase relative permeability} \\
n_p &= \text{number of phases} \\
p_c &= \text{capillary pressure, bar} \\
p_d &= \text{capillary entry pressure, bar} \\
p_j &= \text{phase pressure, bar} \\
p_n &= \text{pressure for non-wetting phase, bar} \\
p_{ref} &= \text{reference pressure, bar} \\
p_w &= \text{pressure for wetting phase, bar} \\
\tilde{q}_j &= \text{phase in/outflux, m}^3\text{/d} \\
r &= \text{residual} \\
s_j &= \text{phase saturation} \\
S_{gr} &= \text{residual gas saturation} \\
S_{or} &= \text{residual oil saturation} \\
S_{wc} &= \text{connate water saturation}
\end{aligned}
$$

u_j = phase velocity, m/d
x_{cj} = component mole fraction in a phase
α_c = physical term of mass accumulation operator, mol/m^3
β_c = physical term of mass convection operator, mol/m^3/cp
Γ^l = geometrical part of transmissibility, cp·m^3/d/bar
λ = capillary exponent
μ_j = phase viscosity, cp
μ_{app} = foam apparent viscosity, cp
ρ_j = phase molar density, mol/m^3
σ_{wg} = water/gas surface tension, N/m
ϕ = effective rock porosity

Acknowledgments

References

Al Ayesh, A. H., Salazar, R., Farajzadeh, R. et al. 2017. Foam Diversion in Heterogeneous Reservoirs: Effect of Permeability and Injection Method. *SPE J.* **22** (5): 1402–402. SPE-179650-PA. https://doi.org/10.2118/179650-PA.

Alcorn, Z. P., Føyen, T., Zhang, L. et al. 2020. CO$_2$ Foam Field Pilot Design and Initial Results. Paper presented at the SPE Improved Oil Recovery Conference, Virtual, 31 August–4 September. SPE-200450-MS. https://doi.org/10.2118/200450-MS.

Alcorn, Z. P., Fredriksen, S. B., Sharma, M. et al. 2019. An Integrated Carbon-Dioxide-Foam Enhanced-Oil-Recovery Pilot Program with Combined Carbon Capture, Utilization, and Storage in an Onshore Texas Heterogeneous Carbonate Field. *SPE Res Eval & Eng* **22** (4): 1449–1466. SPE-190204-PA. https://doi.org/10.2118/190204-PA.

Alverez, J., Rivas, H., and Rossen, W. 1999. A Unified Model for Steady-State Foam Behavior at High and Low Foam Qualities. Paper presented at IOR 1999–10th European Symposium on Improved Oil Recovery, Brighton, UK, 18–20 August. https://doi.org/10.3997/2214-4609.201406323.

Andrianov, A., Farajzadeh, R., Mahmoodi Nick, M. et al. 2012. Immiscible Foam for Enhancing Oil Recovery: Bulk and Porous Media Experiments. *Ind. Eng. Chem. Res.* **51** (5): 2214–2226. https://doi.org/10.1021/ie201872v.

Bascialla, G., Montes, J., Romero, P. et al. 2017. Feasibility of Foam Application in a Giant Mature Field Under Miscible Wag Injection. Paper presented at the Abu Dhabi International Petroleum Exhibition and Conference, Abu Dhabi, UAE, 13–16 November. SPE-188424-MS. https://doi.org/10.2118/188424-MS.

Bikerman, J. J. 1973. *Foams*, Vol. 10. New York, New York, USA: Foams Series, Springer-Verlag.

Boeije, C. S. and Rossen, W. 2015. Fitting Foam-Simulation-Model Parameters to Data: I. Coinjection of Gas and Liquid. *SPE Res Eval & Eng* **18** (2): 264–272. SPE-174544-PA. https://doi.org/10.2118/174544-PA.

Brooks, R. and Corey, T. 1964. *Hydraulic Properties of Porous Media*. Fort Collins, Colorado, USA: Hydrology Papers, Colorado State University.

Castañeda, P., Abreu, E., Furtado, F. et al. 2016. On a Universal Structure for Immiscible Three-Phase Flow in Virgin Reservoirs. *Computat Geosci* **20** (1): 171–185. https://doi.org/10.1007/s10596-016-9556-5.

Chapuis, R. P. and Aubertin, M. 2003. *Predicting the Coefficient of Permeability of Soils Using the Kozeny-Carman Equation*. Report EPM-RT-2003-03, École Polytechnique de Montréal, Montreal, Québec, Canada, January 2003.

Chen, H., Elhag, A. S., Chen, Y. et al. 2018. Oil Effect on CO$_2$ Foam Stabilized by a Switchable Amine Surfactant at High Temperature and High Salinity. *Fuel* **227** (1 September): 247–255. https://doi.org/10.1016/j.fuel.2018.04.020.

Cheng, L., Reme, A., Shan, D. et al. 2000. Simulating Foam Processes at High and Low Foam Qualities. Paper presented at the SPE/DOE Improved Oil Recovery Symposium, Tulsa, Oklahoma, USA, 3–5 April. SPE-59287-MS. https://doi.org/10.2118/59287-MS.

Computer Modelling Group (CMG). 2012. *STARS User's Guide*. Calgary, Alberta, Canada.

Deshpande, S., Shiau, B., Wade, D. et al. 1999. Surfactant Selection for Enhancing Ex Situ Soil Washing. *Water Res* **33** (2): 351–360. https://doi.org/10.1016/S0043-1354(98)00234-6.

Dharma, A. 2013. *Simulation Studies of Foam for Enhanced Oil Recovery*. MS thesis, Delft University of Technology, Delft, The Netherlands.

Dholkawala, Z. F., Sarma, H., and Kam, S. 2007. Application of Fractional Flow Theory to Foams in Porous Media. *J Pet Sci Eng* **57** (1–2): 152–165. https://doi.org/10.1016/j.petrol.2005.10.012.

Eftekhari, A. A. and Farajzadeh, R. 2017. Effect of Foam on Liquid Phase Mobility in Porous Media. *Sci Rep* **7**: 43870. https://doi.org/10.1038/srep43870.

Esene, C., Zendehboudi, S., Aborig, A. et al. 2019. A Modeling Strategy To Investigate Carbonated Water Injection for EOR and CO$_2$ Sequestration. *Fuel* **252** (15 September): 710–721. https://doi.org/10.1016/j.fuel.2019.04.058.

Falls, A., Hirasaki, G., Patzek, T. W. et al. 1988. Development of a Mechanistic Foam Simulator: The Population Balance and Generation by Snap-Off. *SPE Res Eng* **3** (3): 884–892. SPE-14961-PA. https://doi.org/10.2118/14961-PA.

Farajzadeh, R., Andrianov, A., Krastev, R. et al. 2012. Foam-Oil Interaction in Porous Media: Implications for Foam Assisted Enhanced Oil Recovery. *Adv Colloid Interface Sci* **183** (15 November): 1–13. https://doi.org/10.1016/j.cis.2012.07.002.

Fisher, A., Foulser, R., and Goodyear, S. 1990. Mathematical Modeling of Foam Flooding. Paper presented at the SPE/DOE Enhanced Oil Recovery Symposium, Tulsa, Oklahoma, USA, 22–25 April. SPE-20195-MS. https://doi.org/10.2118/20195-MS.

Friedmann, F., Chen, W., and Gauglitz, P. 1991. Experimental and Simulation Study of High-Temperature Foam Displacement in Porous Media. *SPE Res Eng* **6** (1): 37–45. SPE-17357-PA. https://doi.org/10.2118/17357-PA.

Gong, J., Vincent-Bonnieu, S., Kamarul Bahrim, R. Z. et al. 2020. Injectivity of Multiple Slugs in Surfactant Alternating Gas Foam EOR: A CT Scan Study. *SPE J.* **25** (2): 895–906. SPE-199888-PA. https://doi.org/10.2118/199888-PA.

Hosseini-Nasab, S., Douarche, F., Simjoo, M. et al. 2018. Numerical Simulation of Foam Flooding in Porous Media in the Absence and Presence of Oleic Phase. *Fuel* **225** (1 August): 655–662. https://doi.org/10.1016/j.fuel.2018.03.027.

Hussain, A., Amin, A., Vincent-Bonnieu, S. et al. 2017. Effect of Oil on Gravity Segregation in SAG Foam Flooding. Paper presented at IOR 2017–19th European Symposium on Improved Oil Recovery, Stavanger, Norway, 24–27 April. https://doi.org/10.3997/2214-4609.201700342.

Islam, M. and Ali, S. 1988. Numerical Simulation of Foam Flow in Porous Media. Paper presented at the Annual Technical Meeting, Calgary, Alberta, Canada, 11–15 June. PETSOC-88-39-04. https://doi.org/10.2118/88-39-04.

Izadi, M. and Kam, S. 2018. Investigating Supercritical CO_2 Foam Propagation Distance: Conversion from Strong Foam to Weak Foam vs. Gravity Segregation. *Transp Porous Med* **131:** 223–250. https://doi.org/10.1007/s11242-018-1125-z.

Kala, K. and Voskov, D. 2020. Element Balance Formulation in Reactive Compositional Flow and Transport with Parameterization Technique. *Computat Geosci* **24** (2): 609–624. https://doi.org/10.1007/s10596-019-9828-y.

Kam, S. I., Nguyen, Q. P., Li, Q. et al. 2007. Dynamic Simulations with an Improved Model for Foam Generation. *SPE J.* **12** (1): 35–48. SPE-90938-PA. https://doi.org/10.2118/90938-PA.

Kapetas, L., Vincent-Bonnieu, S., Farajzadeh, R. et al. 2015. Effect of Permeability on Foam-Model Parameters–An Integrated Approach from Coreflood Experiments through to Foam Diversion Calculations. Paper presented at IOR 2015–18th European Symposium on Improved Oil Recovery, Dresden, Germany, 14–16 April. https://doi.org/10.3997/2214-4609.201412124.

Katiyar, A., Hassanzadeh, A., Patil, P. et al. 2020. Successful Field Implementation of CO_2-Foam Injection for Conformance Enhancement in the Evgsau Field in the Permian Basin. Paper presented at the SPE Improved Oil Recovery Conference, Virtual, 31 August–4 September. SPE-200327-MS. https://doi.org/10.2118/200327-MS.

Khait, M. and Voskov, D. 2017. Operator-Based Linearization for General Purpose Reservoir Simulation. *J Pet Sci Eng* **157** (August): 990–998. https://doi.org/10.1016/j.petrol.2017.08.009.

Khait, M. and Voskov, D. 2018. Adaptive Parameterization for Solving of Thermal/Compositional Nonlinear Flow and Transport with Buoyancy. *SPE J.* **23** (2): 522–534. SPE-182685-PA. https://doi.org/10.2118/182685-PA.

Khait, M., Voskov, D., and Konidala, G. 2018. Tie-Simplex Parametrization for Operator-Based Linearization for Non-Isothermal Multiphase Compositional Flow in Porous. Paper presented at ECMOR XVI–16th European Conference on the Mathematics of Oil Recovery, Barcelona, Spain, 3–6 September. https://doi.org/10.3997/2214-4609.201802183.

Khait, M., Voskov, D., and Zaydullin, R. 2020. High Performance Framework for Modelling of Complex Subsurface Flow and Transport Applications. Paper presented at ECMOR XVII–17th European Conference on the Mathematics of Oil Recovery, Virtual, 14–17 September. https://doi.org/10.3997/2214-4609.202035188.

Kim, J., Dong, Y., and Rossen, W. R. 2005. Steady-State Flow Behavior of CO_2 Foam. *SPE J.* **10** (4): 405–415. SPE-89351-PA. https://doi.org/10.2118/89351-PA.

Kovscek, A., Patzek, T., and Radke, C. 1995. A Mechanistic Population Balance Model for Transient and Steady-State Foam Flow in Boise Sandstone. *Chem Eng Sci* **50** (23): 3783–3799. https://doi.org/10.1016/0009-2509(95)00199-F.

Lake, L. W., Johns, R., Rossen, W. R. et al. 2014. *Fundamentals of Enhanced Oil Recovery*. Richardson, Texas, USA: Society of Petroleum Engineers.

Law, D.-S., Yang, Z.-M., and Stone, T. 1992. Effect of the Presence of Oil on Foam Performance: A Field Simulation Study. *SPE Res Eng* **7** (2): 228–236. SPE-18421-PA. https://doi.org/10.2118/18421-PA.

Li, B. and Tchelepi, H. A. 2015. Nonlinear Analysis of Multiphase Transport in Porous Media in the Presence of Viscous, Buoyancy, and Capillary Forces. *J Comput Phys* **297** (15 September): 104–131. https://doi.org/10.1016/j.jcp.2015.04.057.

Lotfollahi, M., Farajzadeh, R., Delshad, M. et al. 2016. Comparison of Implicit-Texture and Population-Balance Foam Models. *J Nat Gas Sci Eng* **31** (April): 184–197. https://doi.org/10.1016/j.jngse.2016.03.018.

Mannhardt, K., Novosad, J., and Schramm, L. 1998. Foam/Oil Interactions at Reservoir Conditions. Paper presented at the SPE/DOE Improved Oil Recovery Symposium, Tulsa, Oklahoma, USA, 19–22 April. SPE-39681-MS. https://doi.org/10.2118/39681-MS.

Marfoe, C., Kazemi, H., and Ramirez, W. 1987. Numerical Simulation of Foam Flow in Porous Media. Paper presented at the SPE Annual Technical Conference and Exhibition, Dallas, Texas, USA, 27–30 September. SPE-16709-MS. https://doi.org/10.2118/16709-MS.

Namdar-Zanganeh, M., La Force, T., Kam, S. et al. 2008. Fractional-Flow Theory of Foam Displacements with Oil. Paper presented at ECMOR XI–11th European Conference on the Mathematics of Oil Recovery, Bergen, Norway, 8–11 September. https://doi.org/10.3997/2214-4609.20146361.

Nell, M. 2015. *Oil Foam Interaction: Simulation of Foam Displacement with Oil*. MS thesis, Delft University of Technology, Delft, The Netherlands.

Osei-Bonsu, K., Grassia, P., and Shokri, N. 2017. Relationship between Bulk Foam Stability, Surfactant Formulation and Oil Displacement Efficiency in Porous Media. *Fuel* **203** (1 September): 403–410. https://doi.org/10.1016/j.fuel.2017.04.114.

Osterloh, W. and Jante, M. Jr. 1992. Effects of Gas and Liquid Velocity on Steady-State Foam Flow at High Temperature. Paper presented at the SPE/DOE Enhanced Oil Recovery Symposium, Tulsa, Oklahoma, USA, 22–24 April. SPE-24179-MS. https://doi.org/10.2118/24179-MS.

Patzek, T. and Myhill, N. 1989. Simulation of the Bishop Steam Foam Pilot. Paper presented at the SPE California Regional Meeting, Bakersfield, California, USA, 5–7 April. SPE-18786-MS. https://doi.org/10.2118/18786-MS.

Rognmo, A., Heldal, S., and Fernø, M. 2018. Silica Nanoparticles To Stabilize CO_2-Foam for Improved CO_2 Utilization: Enhanced CO_2 Storage and Oil Recovery from Mature Oil Reservoirs. *Fuel* **216** (15 March): 621–626. https://doi.org/10.1016/j.fuel.2017.11.144.

Rossen, W. R. 1996. Foams in Enhanced Oil Recovery. In *Foams: Theory, Measurements and Applications*, ed. R. K. Prud'homme and S. A. Khan, first edition, 413–464. New York, New York, USA: Routledge.

Rossen, W. 2013. Numerical Challenges in Foam Simulation: A Review. Paper presented at the SPE Annual Technical Conference and Exhibition, New Orleans, Louisiana, USA, 30 September–2 October. SPE-166232-MS. https://doi.org/10.2118/166232-MS.

Rossen, W. and Wang, M. 1999. Modeling Foams for Acid Diversion. *SPE J.* **4** (2): 92–100. SPE-56396-PA. https://doi.org/10.2118/56396-PA.

Schramm, L. L. 1994. *Foams: Fundamentals and Applications in the Petroleum Industry*, Vol. 242. Washington, DC, USA: American Chemical Society.

Shah, S. Y., As Syukri, H., Wolf, K.-H. et al. 2020. Foam Generation in Flow across a Sharp Permeability Transition: Effect of Velocity and Fractional Flow. *SPE J.* **25** (1): 451–464. SPE-195517-PA. https://doi.org/10.2118/195517-PA.

Sharma, B. C., Brigham, W. E., Castanier, L. M. et al. 1997. *CT Imaging Techniques for Two-Phase* and *Three-Phase in Situ Saturation Measurements*. PhD dissertation, Stanford University, Stanford, California, USA.

Tang, J. 2019. *The Effect of Oil on Foam for Enhanced Oil Recovery: Theory and Measurements*. PhD dissertation, Delft University of Technology, Delft, The Netherlands.

Tang, J., Ansari, M. N., and Rossen, W. R. 2019. Quantitative Modeling of the Effect of Oil on Foam for Enhanced Oil Recovery. *SPE J.* **24** (3): 1057–1075. SPE-194020-PA. https://doi.org/10.2118/194020-PA.

Tang, J., Vincent-Bonnieu, S., and Rossen, W. 2018. Experimental Investigation of the Effect of Oil on Steady-State Foam Flow in Porous Media. *SPE J.* **24** (1): 140–157. SPE-194015-PA. https://doi.org/10.2118/194015-PA.

van der Meer, J., Kraaijevanger, J., Möller, M. et al. 2016. Temporal Oscillations in the Simulation of Foam Enhanced Oil Recovery. Paper presented at ECMOR XV–15th European Conference on the Mathematics of Oil Recovery, Amsterdam, The Netherlands, 29 August–1 September. https://doi.org/10.3997/2214-4609.201601850.

Vitoonkijvanich, S., AlSofi, A. M., and Blunt, M. J. 2015. Design of Foam-Assisted Carbon Dioxide Storage in a North Sea Aquifer Using Streamline-Based Simulation. *Int. J. Greenh. Gas Control* **33** (February): 113–121. https://doi.org/10.1016/j.ijggc.2014.11.022.

Voskov, D. V. 2017. Operator-Based Linearization Approach for Modeling of Multiphase Multi-Component Flow in Porous Media. *J Comput Phys* **337** (15 May): 275–288. https://doi.org/10.1016/j.jcp.2017.02.041.

Wang, Y., Voskov, D., Khait, M. et al. 2020. An Efficient Numerical Simulator for Geothermal Simulation: A Benchmark Study. *Appl Energy* **264** (15 April): 114693. https://doi.org/10.1016/j.apenergy.2020.114693.

Zanganeh, M. N., Kam, S. I., LaForce, T. et al. 2011. The Method of Characteristics Applied to Oil Displacement by Foam. *SPE J.* **16** (1): 8–23. SPE-121580-PA. https://doi.org/10.2118/121580-PA.

Zeng, Y., Muthuswamy, A., Ma, K. et al. 2016. Insights on Foam Transport from a Texture-Implicit Local-Equilibrium Model with an Improved Parameter Estimation Algorithm. *Ind. Eng. Chem. Res.* **55** (28): 7819–7829. https://doi.org/10.1021/acs.iecr.6b01424.

Zhang, K., Li, S., and Liu, L. 2020. Optimized Foam-Assisted CO_2 Enhanced Oil Recovery Technology in Tight Oil Reservoirs. *Fuel* **267** (1 May): 117099. https://doi.org/10.1016/j.fuel.2020.117099.

Appendix A—Foam Model

The widely used IT foam model STARS (CMG 2012; Cheng et al. 2000) involves two algorithms, the "dry-out" and "wet-foam" approaches, to illustrate the oil effect on foam strength. In this project, the "wet-foam" algorithm is applied to investigate the effects of water saturation (S_w), shear thinning, and oil saturation (S_o) on foam stability. As shown in Eqs. 4 and 5, gas mobility is modified with the presence of foam by scaling foam-free gas relative permeability.

The water-saturation effect on foam stability, F_6 in the wet-foam model, is defined as

$$F_6 = 0.5 + \frac{\arctan[epdry(S_w - fmdry)]}{\pi}, \quad \text{(A-1)}$$

where *fmdry* and *epdry* are model parameters, representing the limiting water saturation where foam collapses and the abruptness of foam collapse, respectively.

The oil effect on foam strength, F_2 in the wet-foam representation, is defined as

$$F_2 = \begin{cases} 0 & fmoil \leq S_o \leq 1 - S_{wc} - S_{gr} \\ \left(\dfrac{fmoil - S_o}{fmoil - floil}\right)^{epoil} & floil \leq S_o \leq fmoil \\ 1 & S_{or} \leq S_o \leq floil, \end{cases} \quad \text{(A-2)}$$

where *fmoil* is the upper-limiting oil saturation, greater than which foam is destroyed completely, while *floil* is the lower-limiting oil saturation, lower than which oil has no effect on foam. If oil saturation is between these two values, oil destabilizes foam in a nonlinear way.

The shear-thinning function, F_3 in the wet-foam model, is defined as

$$F_3 = \left(\frac{fmcap}{N_{ca}}\right)^{epcap}, \quad \text{(A-3)}$$

where *fmcap* represents a reference capillary number. In STARS, F_3 is limited to values less than or equal to unity. Here we remove that restriction. *epcap* is the exponent representing the importance of shear-thinning effects. With a larger value, foam shows stronger shear-thinning behavior. The capillary number, N_{ca}, is given by

$$N_{ca} = \frac{k\nabla p}{\sigma_{wg}}, \quad \text{(A-4)}$$

where k is absolute permeability, ∇p is the pressure gradient, and σ_{wg} is water/gas surface tension, respectively. The parameters of the relative-permeability and foam model are shown in **Table A-1.**

| Corey Parameters and Fluid Viscosity						Foam Parameters	
k_{rw}^e	k_{ro}^e	k_{rg}^e	n_w	n_o	n_g	*fmmob*	*fmdry*
1	1	1	2	2	2	2,000	0.3
S_{wc}	S_{gr}	S_{or}	μ_w (cp)	μ_o (cp)	μ_g (cp)	*epdry*	*epoil*
0.1	0	0.1	1	5	0.01	32,000	3

Table A-1—Parameter values of the Brooks-Corey relative permeability model and foam model.

## Appendix B—Multiphase Flow with the Effect of Capillarity

Case 1 in Scenario 2 presents a big challenge to our simulations: the numerical results shows oscillations (**Fig. B-1).** Some studies found that extremely small timestep and grid size cannot eliminate these oscillations (Namdar-Zanganeh et al. 2008; Zanganeh et al. 2011; Dharma 2013; Nell 2015). The constant-state point is very close to the critical oil saturation (*fmoil*), and a small variation of saturation can cause the solution to jump across the foam/no-foam boundary, where k_{rg} changes dramatically. This is the reason for the failure of the numerical simulation. Because of the discretization scheme (upwinding), we see this problem in Case 1 of Scenario 2 (Fig. B-1a). In principle, it should be possible to mitigate these oscillations by sufficiently reducing the timestep and grid size (Zanganeh et al. 2011), adding a capillary-diffusion coefficient (Nell 2015; Tang et al. 2019), implementing global/local chops to limit the composition changes during the Newton iterations (Li and Tchelepi 2015), and changing discretization schemes (van der Meer et al. 2016). In our work, we do not test all possibilities to avoid these oscillations. Instead, we eliminate the oscillations by adding a small capillary-diffusion term (Fig. B-1c). We briefly introduce here how the OBL approach handles the capillarity, and further details about simulating the effects of capillarity with the OBL approach will be shown in another publication.
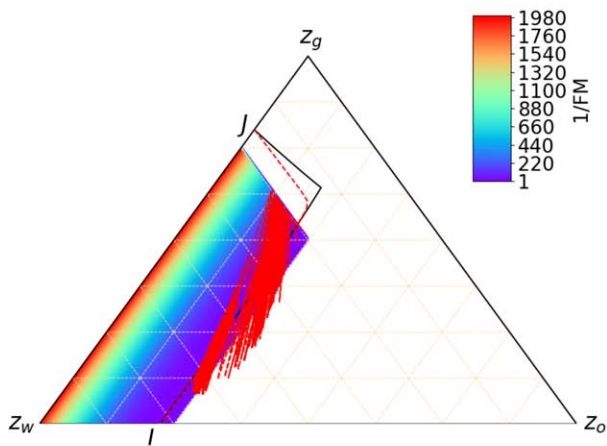
(a) Composition path
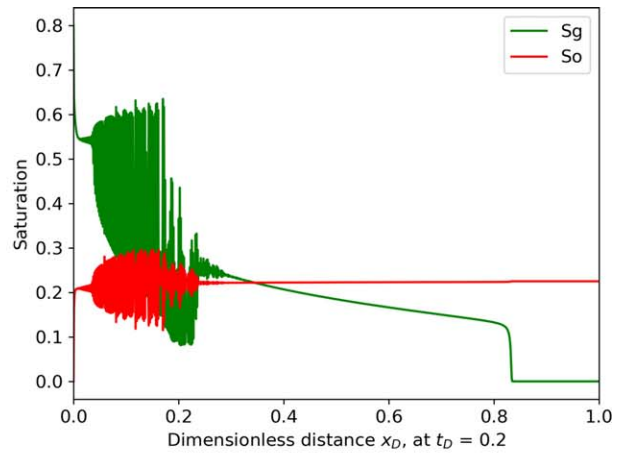
(b) Gas-saturation and oil-saturation profiles
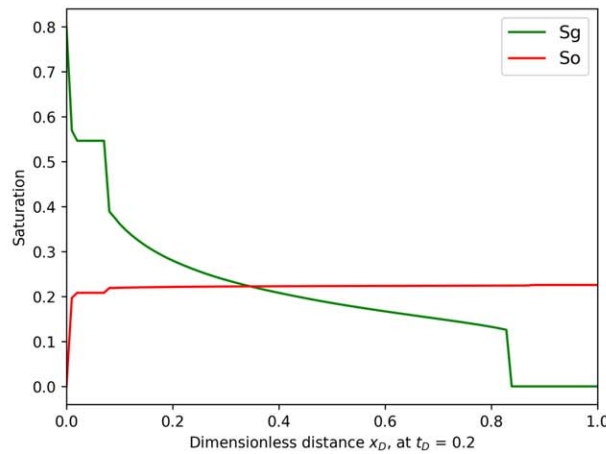
(c) Gas-saturation and oil-saturation profiles with capillary diffusion

Fig. B-1—Illustrations of numerical instability for Case 1 in Scenario 2 in the simulation with 1,000 gridblocks. (a) Composition path from injection condition (*J*) to initial condition (*I*). The black solid line is the analytical solution, and the red dashed line is the OBL solution. (b) Gas-saturation and oil-saturation profiles as a function of dimensionless position x_D at time $t_D = 0.20$ PVI. (c) Gas-saturation and oil-saturation profiles with capillary diffusion introduced to eliminate the oscillations.

Capillary pressure is often expressed as a function of saturation,

$$p_c(s_w) = p_n - p_w, \quad \dots\dots\dots\dots\dots\dots\dots\dots\dots\dots\dots\dots\dots\dots\dots\dots\dots\dots \text{(B-1)}$$

where n and w indicate the nonwetting phase and wetting phase, respectively. The numerical flux in the Delft Advanced Research Terra Simulator is computed using the phase-potential-upwinding strategy (i.e., phase mobilities are selected according to the phase-potential difference). The phase-potential difference p in the absence of gravity between block i and j can be written as

$$\Phi_{p,ij} = p_j - p_{c,j} - (p_i - p_{c,i}). \quad \dots\dots\dots\dots\dots\dots\dots\dots\dots\dots\dots\dots\dots\dots\dots\dots\dots \text{(B-2)}$$

Capillary pressure is treated as one standalone operator that depends only on the physical state. For an n_p-phase system, only $n_p - 1$ capillary pressures are needed for the calculation of phase pressure. To keep the whole system coordinated, the capillary pressure operator of the reference phase is defined as zero. Therefore, n_p capillary pressure operators are introduced in this system. Here, the Brooks-Corey model (Brooks and Corey 1964) is applied for calculation of the capillary pressure operator,

$$p_c(\omega) = p_d \left(\frac{S_w(\omega) - S_{wc}}{1 - S_{wc} - S_{or}} \right)^{-1/\lambda}, \quad \dots\dots\dots\dots\dots\dots\dots\dots\dots\dots\dots\dots\dots\dots\dots\dots \text{(B-3)}$$

where p_d is the capillary entry pressure. The corresponding capillary pressure curves are shown in **Fig. B-2.**
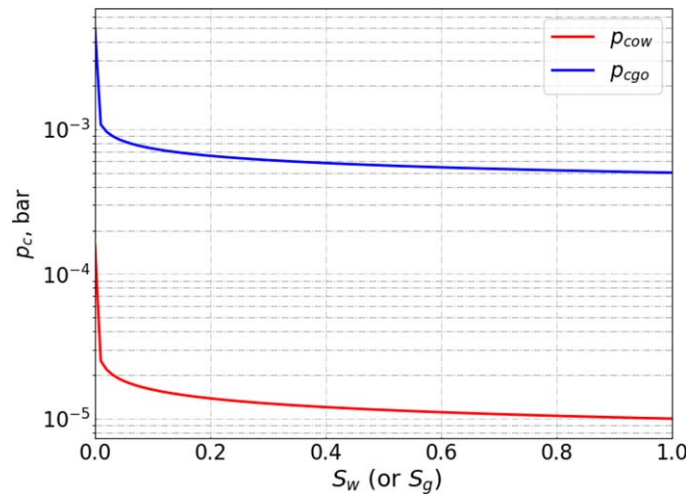
Fig. B-2—Capillary pressure curves used in this study to suppress oscillations. p_{cow} is a function of water saturation (S_w), while p_{cgo} is a function of water saturation (S_g).

Appendix C—Model Regression to the Data by Gradient-Optimization Technique

The relative permeability model implemented here is the Brooks-Corey model (Brooks and Corey 1964). The relative permeability of each phase only depends on its own saturation,

$$k_{r,i} = k_{re,i} \left(\frac{S_i - S_{ir}}{1 - S_{wc} - S_{or} - S_{gr}} \right)^{n_i}, \quad \dots\dots\dots\dots\dots\dots\dots\dots\dots\dots\dots\dots\dots\dots\dots\dots\dots \quad (C\text{-}1)$$

where subscript $i \in \{g, o, w\}$ denotes phases present in the simulation. $k_{r,i}$ and $k_{re,i}$ are phase relative permeability at a certain saturation and at the endpoint, respectively. S_{wc}, S_{or}, and S_{gr} are residual phase saturations.

The modifiers implanted are Brooks-Corey parameters, and there are nine parameters that need to be optimized during the simulation. The objective function tested in the simulation is shown as

$$J(x)_{min} = \sqrt{\sum_{k=1}^{n_p} \sum_{i=1}^{N} [y_k^i(x) - y^{\text{obs}}]^2}, \quad \dots\dots\dots\dots\dots\dots\dots\dots\dots\dots\dots\dots\dots\dots\dots\dots\dots \quad (C\text{-}2)$$

where $y_k^i(x)$ and y^{obs} are phase saturations obtained from the simulation and experiment. The final optimal parameters are shown in **Table C-1.**

Parameters	Value	Parameters	Value	Parameters	Value
k_{rwe}	0.247	S_{wc}	0.197	n_w	3.86
k_{roe}	0.584	S_{or}	0.103	n_o	2.54
k_{rge}	0.830	S_{gr}	0.013	n_g	1.62

Table C-1—Optimal parameter values for Brooks-Corey relative-permeability model.